Estimation of biomass-burning emissions by fusing the fire radiative power retrievals from polar-orbiting and geostationary satellites across the conterminous United States

Fangjun Li[a], Xiaoyang Zhang[a *], David P. Roy[b], Shobha Kondragunta[c]

[a] Geospatial Sciences Center of Excellence, department of Geography, South Dakota State University, Brookings, SD 57007, USA

[b] Center for Global Change and Earth Observations, department of Geography, Environment, & Spatial Sciences, Michigan State University, East Lansing, MI 48824, USA

[c] NOAA/NESDIS/Center for Satellite Applications and Research, College Park, MD 20740, USA

[*]Corresponding author: Xiaoyang Zhang (xiaoyang.zhang@sdstate.edu, Tel: +1 6056886714, Fax: +1 6056885227)

Abstract

Biomass burning is an important source of atmospheric greenhouse gases and aerosols, and its emissions can be estimated using Fire Radiative Power (FRP) retrievals from polar-orbiting and geostationary satellites. Accurate and timely estimation of biomass-burning emissions (BBE) requires high-spatiotemporal-resolution FRP that is characterized by accurate diurnal FRP cycle. This study is to estimate hourly reliable BBE in a 0.25°×0.3125° grid across the conterminous United States (CONUS) to be used in chemical transport models for air quality forecast. To do this, this study for the first time fused FRP retrievals from the Geostationary Operational Environmental Satellite (GOES) with those from Moderate Resolution Imaging Spectroradiometer (MODIS) Collection 6 after GOES FRP was angularly adjusted and was further calibrated against MODIS FRP. The FRP data was obtained from Terra and Aqua MODIS 1km active fire products with fire observations of four times a day and from 4km GOES WF_ABBA (WildFire Automated Biomass Burning Algorithm) fire products for GOES-W (GOES-11 and 15) and GOES-E (GOES-13) with observations every 5-15 minutes across the CONUS from 2011-2015. The diurnal FRP cycles at an interval of 15 minutes for a grid were reconstructed using the ecosystem-specific diurnal FRP climatology and actually available MODIS-GOES fused FRP, which were applied to estimate hourly BBE across the CONUS. The results indicate that the reconstructed diurnal FRP cycle varied significantly in magnitude and shape among 45 CONUS ecosystems. The biomass burning released 717 Gg particulate matter smaller than 2.5 μm in diameter (PM2.5) in the CONUS each year; however, it presented significant temporal (diurnal, seasonal, and interannual) and spatial variations. Finally, the BBE estimates were evaluated using available data sources and compared well (a difference of ~4%) with emissions derived from Landsat burned areas in the western CONUS and with hourly carbon monoxide emissions simulated using a biogeochemical model over the Rim Fire in California (difference < 1%). The BBE estimates showed similar seasonal variation to six available BBE inventories but with variable magnitude.

Keywords

Biomass burning; PM2.5; Fire Radiative Power; MODIS; GOES; CONUS

1. Introduction

Biomass burning from wildfires emits a significant amount of trace gases and aerosols that profoundly impact climate, weather, carbon budget, and public health (Akimoto, 2003; Bowman et al., 2009; Johnston et al., 2016; Kaufman et al., 2002). Global wildfires, on average, annually burn approximately 350 Mha of land (Giglio et al., 2013) and release 2.2 Pg carbon (approximately 23% of fossil-fuel carbon emissions in 2014 (Boden et al., 2017)) into the atmosphere (van der Werf et al., 2017), which has been projected to cause a net global warming of 0.4 K over 20 years by 2026 (Jacobson, 2014). Smoke aerosols (i.e., black carbon and organic carbon) emitted from biomass burning is thought to have cooled the Earth by 0.06-1.30 W m^{-2} in the industrial era (Bond et al., 2013) and warm atmosphere above low-level clouds as well (Ge et al., 2014). Smoke aerosols threaten human health by degrading local to regional air quality. For example, fire-related fine particulate matter smaller than 2.5 μm in diameter (PM2.5) cause several hundreds of thousands of premature deaths worldwide annually (Johnston et al., 2016; Lelieveld et al., 2015). Biomass-burning emissions (BBE) significantly influence the accuracy of atmospheric models and numerical weather models for forecasting air quality and meteorological conditions (Reid et al., 2009; Wang et al., 2009). Accurate and timely estimation of BBE is needed for climate, weather, environment, and air quality applications.

BBE has been estimated since 1980s as the product of burned area, biomass fuel load, the fraction of biomass burned, and emission factors (Seiler and Crutzen, 1980; van der Werf et al., 2017). The degree to which these four parameters are estimated determines the accuracy of BBE estimates. Prior to the satellite era, BBE was highly uncertain and was estimated by statistical extrapolation of results from local experiments to regions and worldwide (Seiler and Crutzen, 1980; Crutzen & Andreae, 1990; Hao et al., 1990), which was briefly reviewed by Wang et al. (2018b). In the satellite era, the burned area and hotspots retrieved from satellite observations have elevated the capability of quantifying BBE. Particularly, with the availability of the global systematically generated Moderate Resolution Imaging Spectroradiometer (MODIS) fire products (Justice et al., 2002), regional and global BBE products have been widely produced, including the Global Fire Emissions Database (GFED) (van der Werf et al., 2017), the Fire Locating and Modeling of Burning Emissions (FLAMBE) (Reid et al., 2009), the Fire INventory from NCAR (FINN) (Wiedinmyer et al., 2011), and the Wildland Fire Emissions Information System (WFEIS) (French et al., 2011). Although large improvements have been achieved in the estimation of burned area (Mouillot et al., 2014; Giglio et al. 2018), it is still challenging to accurately estimate BBE using the conventional bottom-up model. A comparison of several BBE inventories over northern Africa suggested that the bottom-up and top-down based BBE could differ by a factor of ~10 (Zhang et al., 2014). This is due to the fact that burned areas are often underestimated by moderate-resolution satellites (Boschetti et al., 2004; Kasischke et al., 2011), and fuel loadings are static and may differ by more than 35% among different fuel datasets (Zhang et al., 2008).

Retrieval of the fire-released radiative energy from satellite radiance provides alternative ways to estimate BBE. Controlled fires experiments in laboratory and landscape demonstrated that the instantaneous radiative energy or Fire Radiative Power (FRP) is related to the rate of biomass combustion, and the total biomass combusted in a fire event is a function of the temporal integration of FRP, termed Fire Radiative Energy (FRE), and FRE biomass combustion coefficient (FBCC) (Freeborn et al., 2008; Hudak et al., 2016; Kremens et al., 2012; Wooster, 2003; Wooster et al., 2005). This empirical relationship was also confirmed in wildfires based on surface biomass consumption and satellite-derived FRP and emissions retrievals (Konovalov et al., 2014; Li et al., 2018b), in which FRP is retrieved from radiances of fire pixel and non-fire ambient background at 4-μm band (Wooster et al., 2003). The relationship has been frequently used to estimate regional to global BBE using FRP retrievals from polar-orbiting satellites and geostationary satellites (Ellicott et al., 2009; Kaiser et al., 2012; Roberts et al., 2009; Vermote et al., 2009; Zhang et al., 2012). For instance, daily global BBE is operationally produced using FRP retrievals from MODIS and global geostationary satellites in the Quick Fire Emissions Dataset (QFED) (Darmenov & Silva, 2015), the Global Fire Assimilation System (GFAS)(Kaiser et al., 2012), and the Global Geostationary Satellite Biomass Burning Emissions Product (GBBEP-Geo) (Zhang et al., 2012). Another approach is to relate BBE rates directly to FRP using smoke emission coefficients (Freeborn et al., 2008; Ichoku & Kaufman, 2005). Smoke emission coefficients in a 0.1° grid globally are available in the Fire Energetics and

Emissions Research (FEER) product, which can be used to convert FRP to the rate of biomass-burning emissions (Ichoku & Ellison, 2014). These smoke emission coefficients have been further refined based on MODIS Aerosol Optical Depth (AOD) and Meteosat SEVIRI (Spinning Enhanced Visible and Infrared Imager) FRP retrievals and applied to estimate BBE across Africa continent (Mota & Wooster, 2017).

The FRP-based BBE estimates are sensitive to the spatiotemporal resolution of the satellite-based FRP data. Sensors onboard the geostationary satellites (e.g., Meteosat SEVIRI and Geostationary Operational Environmental Satellite (GOES-11, 13, and 15) Imager) generally observe fires once every 5-15 minutes. The high-temporal FRP retrievals enable to establish diurnal FRP variation (cycle) to estimate FRE and BBE at an hourly-to-daily resolution. However, their coarse spatial resolution (e.g., nominal 4 km at nadir for GOES) limits the capability of detecting small and cool fires (e.g., SEVIRI is unable to detect fires with FRP < 50 MW (Roberts & Wooster., 2008)), which could result in underestimation of FRE by 50% (Freeborn et al., 2009) and BBE by a factor of up to four (Roberts et al., 2009; Zhang et al., 2012). On the other hand, the polar-orbiting MODIS onboard Aqua and Terra is able to sense relatively smaller and cooler fires (e.g., fire pixel with FRP > 10 MW (Roberts & Wooster., 2008)) due to higher spatial resolution of MODIS (nominal 1 km) than geostationary sensors. However, each MODIS sensor only provides observations for the same location twice a day but no fire observation due to cloud obscuration and orbital gaps at low latitudes (Wang et al., 2018b). Thus, the polar-orbiting sensors (e.g., MODIS) are incapable of characterizing the diurnal FRP variation at hourly resolution. Because fires have temporal fluctuations in fire radiative power, the FRE estimated by numerical integration of satellite FRP measurements is sensitive to FRP undersampling during temporal gaps between two-successive fire observations (Boschetti & Roy, 2009; Kumar et al., 2011). In summary, present geostationary and polar-orbiting sensors have different limitations in characterizing the diurnal FRP cycle accurately. Note that diurnal FRP cycle here is referred to as the diurnal variation of FRP per grid cell, which differs from the term of diurnal fire cycle that represents the diurnal variation in the total number of active fire detections in a given region (Giglio, 2007).

Two general strategies have been attempted to derive high-spatiotemporal-resolution FRP. The first is to approximate diurnal FRP cycles with predefined Gaussian functions, and fit them to MODIS FRP retrievals (Andela et al., 2015; Ellicott et al., 2009; Konovalov et al., 2014; Vermote et al., 2009). These predefined Gaussian functions may work well for some particular regions rather than the continental to global extents because diurnal FRP cycle varies with fuel types and seasons (Andela et al., 2015; Roberts et al., 2009). The second strategy is to predict the MODIS-equivalent FRP estimates from 15-minute SEVIRI FRP retrievals using the optimized SEVIRI-to-MODIS FRP ratio (Freeborn et al., 2009). However, derivation of the optimized FRP ratio requires a large number of samples cumulated in large spatiotemporal windows (i.e., 5°grid and 15 min, or 1°grid and one month) (Freeborn et al., 2009) that hardly meet the requirements of operational and near-real-time emissions inventories (Andela et al., 2015).

This study is to develop a new algorithm to estimate hourly BBE at a 0.25° latitude by 0.3125° longitude grid across the conterminous United States (CONUS) by fusing FRP from Terra and Aqua MODIS and GOES-E and GOES-W observations. This dataset with the specified spatiotemporal resolution is to serve as emissions input in chemical transport models (e.g. GEOS-CHEM) (Bey et al., 2001; Eastham and Jacob, 2017) and in NOAA (National

Oceanic and Atmospheric Administration) Environmental Modeling System (NEMS) for aerosol forecasting (Lu et al., 2016; Wang et al., 2018a).

2. Methodology

Estimation of hourly BBE across the CONUS was conducted in the following steps. First, an empirical model was developed to adjust GOES FRP retrievals at large view zenith angles (VZA) and the adjusted GOES FRP values were further calibrated against and fused with MODIS FRP retrievals. Second, the calibrated GOES FRP was applied to establish the diurnal FRP climatology for 45 ecosystems at a grid level. Third, the fused FRP estimates were then fitted to the ecosystem-specific diurnal FRP climatology to reconstruct diurnal FRP cycles at a 15-minute interval in a grid that were applied to estimate hourly BBE of PM2.5 and carbon monoxide (CO) in a grid. Finally, the BBE estimates were evaluated and validated.

2.1. Fire radiative power from polar-orbiting and geostationary satellites

2.1.1. MODIS FRP

The MODIS active fire products provide fire detections at the satellite overpass times (Giglio et al., 2016). Terra and Aqua respectively cross the equator at approximately 10:30 AM and 1:30 PM local time during daytime and 10:30 PM and 1:30 AM during nighttime. The MODIS Level 2 active fire products (abbreviated MOD14 for Terra and MYD14 for Aqua) contain for each fire pixel the detection time, geographical coordinate, confidence (low, nominal, and high), fire radiative power (units: MW per pixel), brightness temperature at the MODIS band 21 (3.660-3.840 μm) and band 31 (10.780-11.280 μm), and average brightness temperature of the surrounding non-fire pixels at bands 21 and 31 (Giglio, 2015). FRP estimates in MODIS Collection 6 (C6) active fire product are retrieved following the method developed by Wooster et al. (2003) using the radiances of a fire pixel and ambient non-fire pixels at the band 21, and the area of the fire pixel (Giglio et al., 2016).

This study obtained the MODIS C6 Level 2 active fire products (MOD14 and MYD14) for the period of 2011-2015 from NASA Level-1 and Atmosphere Archive & Distribution System (LAADS) (https://ladsweb.modaps.eosdis.nasa.gov/). This product is defined in the MODIS sensing geometry (a 5-minute granule) that covers an area of approximately 2340 by 2030 km along the scan and track directions, respectively. The MODIS scans 10 1-km lines per mirror rotation over ±55°. The pixel dimension increases from 1 km at nadir to 2.01 km and 4.83 km along the track and scan directions at the scan edge, respectively, which results in oversampling between adjacent scans by up to 50% from the scan angles of 24° to scan edge (Wolfe et al., 2002; Wolfe et al., 1998). As a result, fires can be duplicately detected (Freeborn et al., 2014; Peterson et al., 2013).

The inter-scan duplicate fire detections were corrected in this study using the approach proposed by Li et al. (2018a). Specifically, fire pixels were considered as duplicate detections in consecutive scans (one detection per scan) if they met the following conditions: (1) Fires were detected at the same satellite view angles. (2) Time difference between any two detections was less than 8 seconds because the same point on the Earth surface could be sensed by up to three temporally MODIS adjacent scans at the scan edge during a time period of 4.431seconds (~1.477 seconds per scan × 3 scans) (Wolfe et al., 2002). (3) The distance between the centers of any pair of fire detections was shorter than the along-track dimension of the fire pixels because adjacent scans primarily overlapped each other along the track direction. For each pair of duplicate detections, one of them remained while the other was removed, in which the average FRP was used for the retained detection. Further, the duplicate fire detections can also result from the triangle-shaped point spread function (PSF) of MODIS (Freeborn et al., 2014) in the along-scan direction, which were not corrected in this study because an effective algorithm is not available. Additionally, the MODIS FRP estimates were adjusted using a published adjustment factor (unitless) that was defined as a function of the MODIS scan angle (Li et al., 2018b; Freeborn et al., 2011) to mitigate the underestimation of MODIS FRP at off-nadir view angles.

2.1.2. GOES FRP

The WildFire Automated Biomass Burning Algorithm (WF_ABBA Version 65) active fire product is produced from observations by the Imager sensor onboard the GOES satellites located at 135° W (GOES-W) and 75° W (GOES-E) above the equator, respectively (Schmidt and Prins, 2003). The pixel size in GOES-W (GOES-11 and 15) and GOES-E (GOES-13) increases from 4 to 8 km as the associated view zenith angle (VZA) varies from 30° to 70° across the CONUS. On routine-scanning schedule, the GOES-W senses the central and western CONUS every 5-15 minutes (the 0th, 10th, 15th, 30th, 40th, and 45th minute of every hour approximately), and the GOES-E observes the whole CONUS every 15 minutes (the 0th, 15th, 30th, and 45th minute of every hour approximately) (http://www.ospo.noaa.gov/Operations/GOES/schedules.html). The WF_ABBA detects active fires from all these observations. In WF_ABBA, false alarms due to cloud impacts, very large VZA, and sensor noise are reduced by applying a temporal filter that considers a new fire pixel as a false alarm if it has been detected less than twice during the past 12 hours (Schmidt and Prins, 2003). The GOES WF_ABBA product provides, for each fire pixel, fire location (longitude and latitude), time, FRP, VZA, pixel size, brightness temperature at 4 µm and 11 µm bands, fire temperature, fire size, ecosystem type, and quality flag. The quality flag is divided into six categories: flag 0 – a good quality fire detection, flag 1 – a fire detection with saturated brightness temperature of the 4-µm band, flag 2 – a fire detection contaminated by clouds or thick smoke plumes, flag 3 – a high possibility fire detection, flag 4 – a moderate possibility fire detection, and flag 5 – a low possibility fire detection. FRP is not retrieved for a detection classified as flags 1, 2, or 5. The ecosystem type for a fire pixel is determined based on the United States Geological Survey (USGS) Global Land Cover Characterization (GLCC) data set, which contains 100 ecosystem types globally and 45 primary ecosystems across the CONUS. The GLCC was generated using 1-km AVHRR (advanced very high resolution radiometer) data from April 1992 to March 1993 (Brown et al., 1999).

This study obtained the filtered GOES WF_ABBA active fire product for the period of 2011-2015 from NOAA (http://satepsanone.nesdis.noaa.gov/pub/FIRE/forPo/). Note that the WF_ABBA fire data from July to August 2012 was missing due to the failure of collecting it from NOAA operational website so that the analyses for the year 2012 were excluded. Hereafter, the period of 2011-2015 represents 2011, 2013, 2014, and 2015. This product contains fire detections from GOES-W (GOES-11, replaced by GOES-15 since December 2011) and GOES-E (GOES-13). Approximately 56% of GOES fire detections from 2011 to 2015 were classified as low possibility fire detections (flag 5) which were false alarms in most cases. Therefore, fire pixels with quality flags of 0, 1, 2, or 3 were used and a fire pixel categorized as flag 4 or 5 was considered only if it was detected at least three times per day or at least once with a flag value < 3. Thus, FRP was obtained from observations with flags 0, 3 and 4 while fire duration was determined based on the all the selected fire detections.

2.2. Adjustment of GOES FRP at large view zenith angles

An empirical model was established using GOES-W FRP and GOES-E FRP to adjust the variation of GOES FRP with satellite view zenith angles. It is because FRP at large VZA might be influenced by the increase of radiance contribution from non-fire background large pixels (Schroeder et al., 2010). To do this, GOES-W FRP and GOES-E FRP were first compared to ensure their equivalence by selecting the contemporaneous fire pixels that were detected by these two satellites within ±5 minutes in a 0.1° grid (~7 - 10 km across latitudes 10° - 50°). The comparison was conducted in two steps. First, all spatiotemporally coincident fire detections were obtained if the VZA was the same from GOES-W and GOES-E during 2013 - 2014 in order to verify the similarity of their FRP retrievals. These fire detections were only available within 0.1° grids around the105° W longitude line with a VZA varying from 40° - 65°. The selected samples indeed demonstrated that FRP observations from the two GOES satellites were significantly correlated (R^2=0.8) and approximately equivalent, with a difference of ~10% (Fig. 1). The small difference could be associated with effects of sub-pixel features and different atmospheric paths between two GOES sensors on retrieval of GOES FRP (Peterson et al., 2013; Peterson and Wang, 2013).

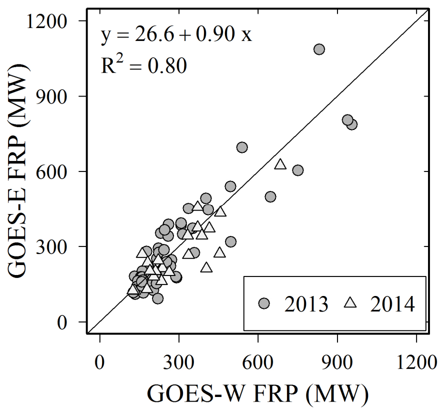

Fig. 1. Comparison of GOES-E FRP with GOES-W FRP for coincident detections (within ±5 minute) collected within 0.1° grids around the 105° W longitude line from 2013 to 2014. The solid line is the 1:1 line.

Second, the contemporaneous fire detections were selected from GOES-W with VZA ranging from 40° to 50° (pixel size from 4.8 to 5.5 km) and GOES-E with VZA varying from 30° to 70° (pixel size from 4 to 8 km) in order to quantify the FRP variation with VZA. Considering GOES-W FRP as a reference and ignoring the small variation of VZA-related pixel size, the ratio of GOES-E to GOES-W FRP was compared to the VZA variation from 30° to 70° (Fig. 2). Then the empirical model was established as:

$$R(\theta) = \frac{FRP_E}{FRP_W} = a + \frac{b}{c\theta + d} \quad (1)$$

where R(θ) is the ratio of GOES-E FRP (FRP_E) to GOES-W FRP (FRP_W), θ is GOES-E VZA (radian), and the parameters (a, b, c, and d) are coefficients obtained by fitting median FRP ratio (Fig. 2).

The fitted model shows that GOES FRP is almost constant if VZA ≤ 50° (Fig. 2). This verifies the assumption that GOES-W FRP variation within VZA of 40° - 50° is negligible. Further, the coefficient of determination (R^2=0.8) demonstrates the model is well established and GOES FRP with VZA < 50° does not need to be adjusted.

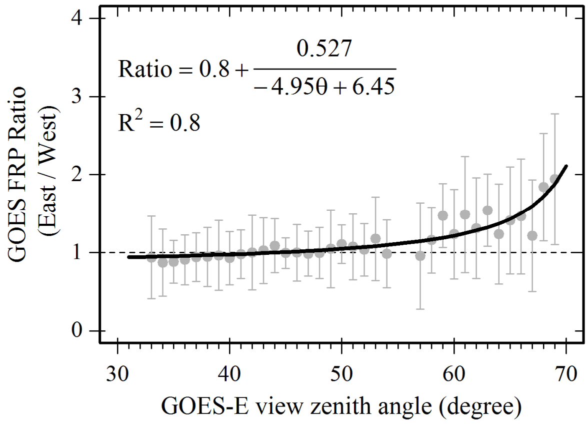

Fig. 2. FRP ratio of GOES-E to GOES-W as a function of GOES-E VZA. The filled gray cycles are the median ratio at every 1-degree VZA from 30° to 70°, and one standard deviation was added as error bars. The black solid line is the fitted model and the dashed line is the FRP ratio with a value of 1.0.

Giving that GOES-E FRP and GOES-W FRP are approximately equivalent at the same VZA as demonstrated in Fig. 1, the FRP influenced by VZA could be adjusted using the equation (2) that was deduced from equation (1):

$$FRP_{adj} = \frac{FRP_\theta}{R(\theta)} \quad (2)$$

where FRP_{adj} is the adjusted FRP and FRP_θ is the GOES fire FRP observed at VZA of θ. For convenient purpose, hereafter the adjusted GOES FRP is simply referred to as GOES FRP.

2.3. Calibration of GOES FRP against MODIS FRP

GOES FRP was calibrated by comparing with MODIS FRP at a 0.25°×0.3125° grid. It is well demonstrated that the MODIS sensor has better fire detection capability than GOES due to higher spatial resolution, which enables MODIS to detect relatively smaller and cooler fires (Schroeder et al., 2010; Xu et al., 2010). Thus, two different approaches were separately applied to calibrate GOES FRP in grids based on the two cases whether contemporaneous MODIS FRP observations within ±6 minutes of GOES observations were available or not available. Specifically, the MODIS FRP and the VZA adjusted GOES FRP (FRP_{adj}) with the same GLCC ecosystem observed at a given time in a grid cell were first aggregated, respectively, which were referred to as grid GOES FRP (FRP_{GOES}) and MODIS FRP (FRP_{MODIS}) hereafter. When contemporaneous FRP_{GOES} and FRP_{MODIS} were available in a grid, the following calibration was applied:

$$FRP_{cal}(t) = FRP_{GOES}(t) + FRP_{offset}(t) \tag{3}$$

where t is time of GOES observation during a day; $FRP_{cal}(t)$ is the calibrated grid GOES FRP; $FRP_{GOES}(t)$ is the grid GOES FRP; and $FRP_{offset}(t)$ is an FRP offset value at time t interpolated linearly from the difference between contemporaneous grid MODIS and GOES FRP for that day (Li et al., 2018b).

The contemporaneous MODIS and the GOES FRP observations were not available in considerable grids. Thus, the following calibration was applied:

$$FRP_{cal}(t) = \beta_0 + \beta_1 FRP_{GOES}(t) \tag{4}$$

where $FRP_{cal}(t)$ and $FRP_{GOES}(t)$ are the same as in equation (3); β_0 and β_1 are calibration coefficients.

The coefficients β_0 and β_1 were derived by comparing contemporaneous MODIS FRP and VZA adjusted GOES FRP in 30m Landsat burned areas. To do this, we obtained 628 fire events for the time period between 2013 and 2015 across the CONUS from the Monitoring Trends in Burn Severity (MTBS) project (http://www.mtbs.gov/) (Eidenshink et al., 2007), where the size of burned area ranged from 2.3 to 884.4 km^2. The Landsat burned areas were stratified based on the dominant land cover type: forests, shrublands, savannas, grasslands, and croplands, each of which was reclassified from GLCC ecosystems by a cross-walking method. For each burned area, the associated contemporaneous MODIS FRP and VZA adjusted GOES FRP were calculated and applied to derive land-cover specific calibration coefficients using a simple ordinary least squares regression (Table 1).

Table 1. Calibration coefficients for five land cover types

Land cover type	Calibration coefficients		r^2	Number of burned areas
	β_0	β_1		
Forest	328	1.96	0.82	304
Shrublands	185	1.43	0.86	55
Savannas	150	1.76	0.94	46
Grasslands	158	1.05	0.65	176
Croplands	84	1.09	0.85	47

2.4. Fusion of MODIS FRP with the calibrated GOES FRP

The calibrated grid GOES FRP was fused with the grid MODIS FRP. The fusion was performed at a 0.25°×0.3125° grid in each 15-minute bin during a day using the following equation:

$$FRP_{fused} = w_1 FRP_{MODIS} + w_2 FRP_{cal} \quad (5)$$

where FRP_{fused} is the fused grid FRP within a 15-minute bin; FRP_{MODIS} and FRP_{cal} are respectively the grid MODIS FRP and the calibrated grid GOES FRP; and w_1 and w_2 are fusion weights in which w_1=1 and w_2=0 if FRP_{MODIS} was valid, and w_1=0 and w_2=1 if only FRP_{cal} was available.

This fusion algorithm was visually illustrated in Fig. 3. The VZA adjusted GOES FRP without calibration is on average 73% smaller than the fused FRP in a 15-minute bin, but the MODIS FRP aligns very well with the fused FRP. This demonstrates that the fused FRP could characterize diurnal FRP cycle effectively.

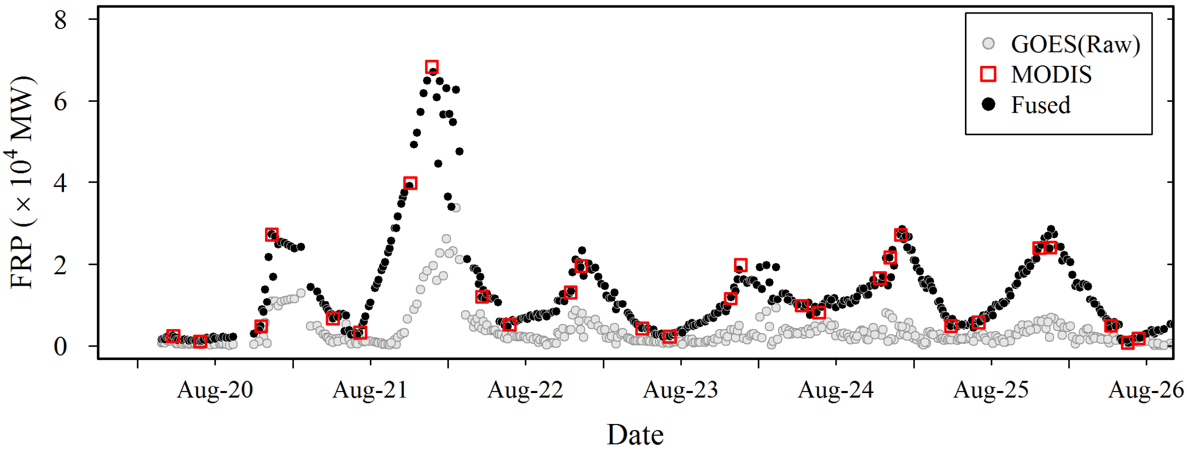

Fig. 3. Diurnal variations of GOES FRP (not calibrated, denoted as "raw"), MODIS FRP, and fused FRP (FRP_{fused}) over the Rim Fire from 20 to 26 August 2013. Each GOES FRP sample is the total FRP aggregated from the VZA-adjusted grid GOES FRP within fire perimeter at a GOES observing time, and each MODIS FRP sample is the total FRP aggregated from grid MODIS FRP within fire perimeter.

2.5. Reconstruction of diurnal FRP cycles

2.5.1. Establishment of diurnal FRP climatology

The climatology of diurnal GOES FRP was established to predict FRP for temporally missing observations caused by obscuration of clouds, very thick smoke plume, and detection capability of sensors. Because fire properties and behaviors could differ greatly among ecosystems, which are related to fuel characterizations (availability, amount, and spatial distribution, etc.) and thus are linked to fire activity (e.g., fire type and intensity) (Pausas and Ribeiro, 2013), the diurnal FRP climatology was investigated separately for different GLCC ecosystems. Since more than 95% of GOES active fires were observed in 18 of 45 primary GLCC ecosystems across the CONUS, the related 18 ecosystems were selected separately, and the rest (37 types) was combined into one type. Thus, a total of 19 ecosystem types were divided. The diurnal FRP climatology for each ecosystem was generated based on the following steps.

First, for each 15-minute bin, the calibrated GOES FRP values in each grid cell across the CONUS from 2011 to 2015 were grouped at an interval of every 20MW. Next, the probability density of FRP observations in each group was estimated using a kernel density estimation approach (Venables and Ripley, 2002). The groups with GOES FRP density less than 0.05% of the maximal group density within a specific 15-minute bin were then removed because small samples could greatly bias FRP estimates. Finally, the mean FRP was calculated from the remaining GOES FRP values every 15 minutes, which was used to determine the diurnal FRP climatology for each ecosystem. As a result, diurnal FRP climatology was obtained for the 19 GLCC ecosystems separately (Fig. 4), which generally presents a trough during 6:00-8:00 and a peak during 13:00-16:00 (local time). The diurnal variations of FRP climatology are large in the cool conifer forest ecosystem and shrub-related ecosystems but are small in the deciduous broadleaf forests, mixed forests, and crop-related ecosystems. Although the diurnal FRP climatology could vary monthly in the magnitude, it shows a very similar diurnal shape based on the example in the cool conifer forest (not presented here). Thus, the seasonal variation in diurnal FRP climatology was not considered in this study.

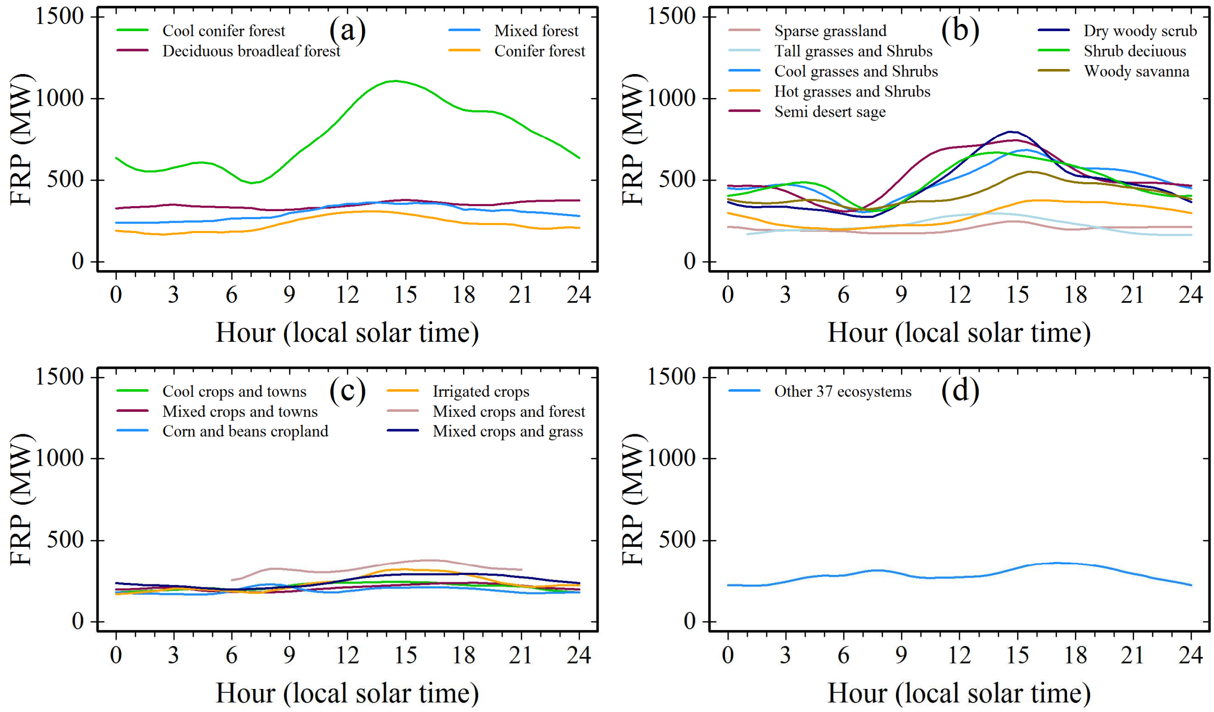

Fig. 4. Ecosystem-specific diurnal FRP climatology across the CONUS: (a) four GLCC forest ecosystems, (b) eight GLCC grass, shrub, and savanna ecosystems, (c) six GLCC crop ecosystems, and (d) the combination of other 37 GLCC ecosystems.

The climatological monthly maximum diurnal burning duration (MMDBD, hours) was further calculated, which was used to quantify the potential fire duration during a day. The MMDBD was defined as the longest period that active fires could be detected by satellites during a day, which represents the temporal boundaries of the satellite detectable fires. The MMDBD could vary with fuel, fire weather, and fire types. The climatological MMDBD was calculated by extracting the mean timings of the earliest and latest ten GOES fire detections (including fire detections without FRP retrievals) during 2011-2015. As a result, the MMDBD was also calculated for the 19 ecosystem types.

In addition, the hourly and monthly possibility of GOES fire detection was also derived for the 19 ecosystem types. It is the percentage of fire detections sensed by GOES every hour during a day or every month in a year, which indicates the diurnal and seasonal possibilities of the occurrences of fires.

The climatology of both the MMDBD and the hourly and monthly possibility of GOES fire detections were illustrated using an example in three GLCC ecosystems showing large variations (Fig. 5). These statistical data were used to determine the potential burning duration of a fire as described in Section 2.5.2.

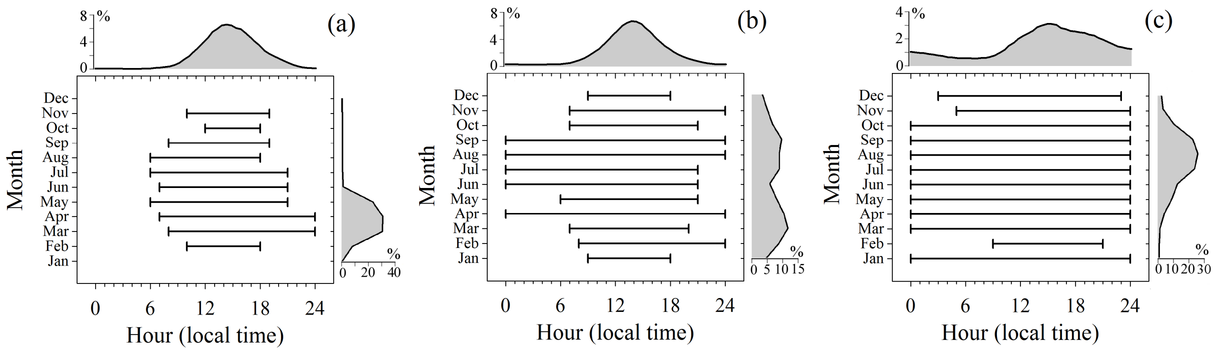

Fig. 5. Monthly maximum diurnal burning duration (MMDBD) and hourly and monthly density of GOES active fire detections in three ecosystems: (a) tall grasses and shrubs, (b) mixed forests, and (c) cool conifer forests. The black lines are MMDBD, and the horizontal and vertical densities are proportions (in percentage) of GOES active fire detections at an interval of an hour and a month, respectively.

2.5.2. Reconstructing diurnal FRP cycles

Diurnal FRP cycles were reconstructed from the fused grid FRP and diurnal FRP climatology at a 0.25°×0.3125° grid for each ecosystem based on the following three steps:

1. The fused grid FRP (FRP_{fused}, see section 2.4) was fitted to the FRP climatology in the same ecosystem by shifting an offset (Zhang et al., 2012). By assuming that the shapes of diurnal FRP cycles were similar for a given ecosystem, the offset was calculated using a least square method from a set of FRP_{fused} observations and the corresponding values on the diurnal FRP climatology curve. Thus, the shifted FRP climatology represents the potential diurnal FRP curve for the FRP_{fused} observations.
2. Temporal gaps were determined using actual FRP_{fused} observations and climatological values of MMDBD and hourly and monthly density of active fire detections. A temporal FRP gap was the period of one or more consecutive 15-minute bins in which FRP_{fused} observations were not available. Because fires (except for large forest fires) could only burn continuously a few hours instead of an entire day in a grid, the length of a temporal gap was determined based on the ecosystem-specific MMDBD and the hourly and monthly possibility of GOES fire detections. The possibility of fire occurrence generally is stronger in the early afternoon

and during fire seasons when fire weather is more favorable for combustion, and more fuels are available to burn (Giglio et al., 2006; Giglio 2007). Therefore, a fire most likely burns longer during the time periods with the stronger possibility of fire detections than the other time periods. For each FRP_{fused} observation, a fire was assumed to burn continuously for:

(a) one hour before and after the fire observation (with and/or without FRP retrievals), respectively, if the observation was collected in the early afternoon (13:00-15:00 local solar time) during fire seasons;

(b) 30 minutes if the observation was collected in other hours during fire and non-fire seasons, and it was located within MMDBD (section 2.5.1);

(c) 15 minutes if the observation was located outside of MMDBD. This is because a fire seldom occurs (or too small/cool to be detected) in hours beyond the MMDBD.

3. Missing FRP values in temporal gaps were interpolated using the valid fused FRP or predicted using the shifted FRP climatology. If a gap was less than one hour, the missing FRP values were linearly interpolated from the fused FRP of their nearest neighbors at the two sides. Otherwise, the shifted FRP climatology was selected as predictions. Finally, a reconstructed diurnal FRP cycle was obtained from a combination of actual FRP_{fused} observations and the interpolated and predicted FRP_{fused} in temporal gaps.

The process of reconstructing diurnal FRP was demonstrated using four different cases of fires occurred in cool conifer, conifer, dry woody scrub, and cropland dominated grids (Fig. 6). Gaps (yellow filled triangles) were mainly resulted from fire observations without FRP retrievals due to the obscuration of clouds and thick smoke plumes, particularly in southeastern (e.g., Fig.6b) and western CONUS (e.g., Fig.6a,c). FRP values in gap length less than one hour (red open cycles) were linearly interpolated while the values in longer gaps (red filled triangles) were predicted using shifted FRP climatology.

Furthermore, a simulation was conducted to evaluate the performance of the climatology-based method in reconstructing diurnal FRP cycle in a well-observed fire that occurred in cool conifer forest on 19 August 2013 (37.0°N, 119.06°W). Specifically, 10% of the valid fused FRP observations during a day were randomly extracted as good observations and the rest observations were assumed as gaps to reconstruct the diurnal FRP cycle based on the diurnal FRP climatology, which was applied to calculate FRE. This process was repeated 1000 times. The same simulation was also conducted using 20% and 30% of all the valid observations. The result shows that the FRE on average based on the simulated diurnal FRP cycle is very similar to the FRE estimated using all valid observations with a difference of 0.34 ± 17%, 0.1 ± 14%, and 0.01 ± 10%, for 10%, 20%, and 30% of all the valid observations, respectively. This simulation suggests that reconstruction of diurnal FRP cycle based on the climatologic FRP performs well.

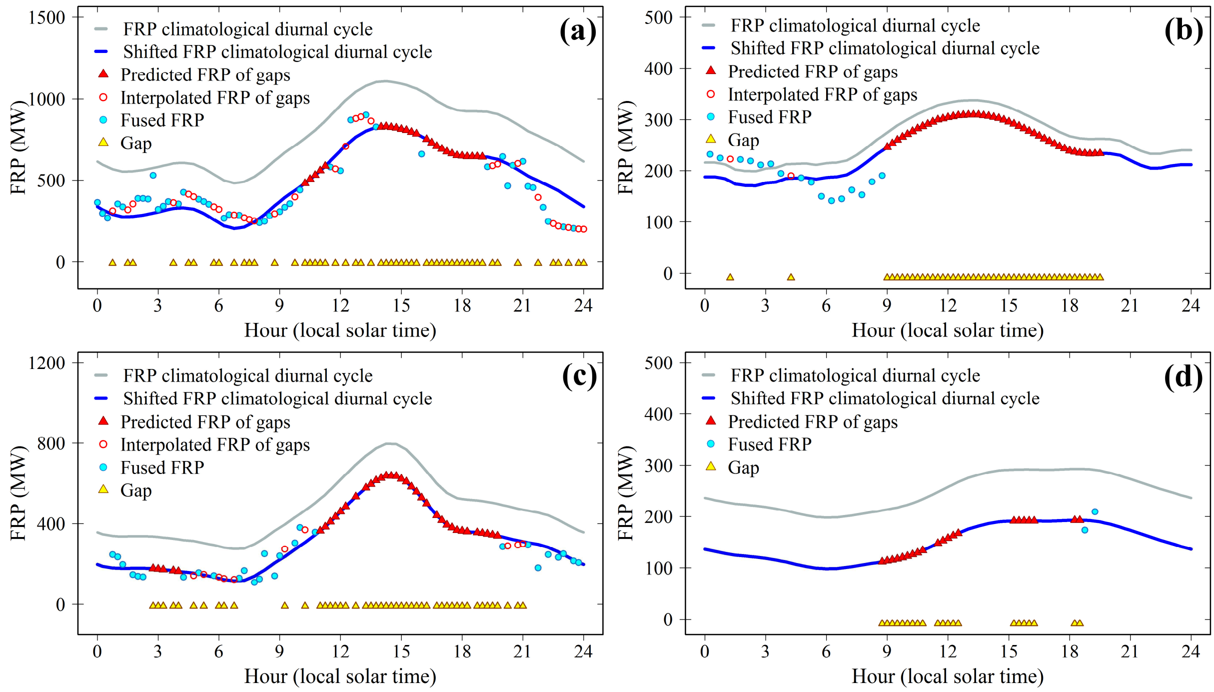

Fig. 6. An example of reconstructing diurnal FRP cycles using the fused FRP observations and FRP climatology for fires burned in four different ecosystems. (a) Cool conifer fire on 2 August 2014 (41.375°N, 122.968°W) in California, (b) Conifer fire on 3 July 2011 (29.5°N, 81.563°W) in Florida, (c) Dry woody scrub fire on 2 June 2014 (33.5°N, 110°W) in Arizona, and (d) cropland fire on 19 April 2014 (47.75°N, 111.875°W) in Montana.

2.6. Estimation of FRE and biomass-burning emissions

FRE was estimated for each grid cell from diurnal FRP cycles. Fires in each 15-minute bin were assumed to burn consistently with an FRP_{fused} value, so that the total hourly FRE in a grid was estimated as:

$$FRE = \sum_{i=1}^{p} FRE_i = \sum_{i=1}^{p}\left[\sum_{j=1}^{q}(FRP_{fused}(i,j)\times 900)\right] \qquad (6)$$

where *FRE* is the hourly fire radiative energy (FRE), FRE_i is hourly GOES-MODIS FRE in the *i*th ecosystem, *p* (p=19) is the number of ecosystems where active fires were detected in a grid by GOES and/or MODIS, $FRP_{fused}(i, j)$ is the reconstructed diurnal fire radiative power (MW) in the *j*th 15-minute bin (900 seconds) and the *i*th ecosystem, and *q* (q=4) is total number of 15-minute bin within one hour.

The FRE estimated from diurnal FRP_{fused} cycles is referred as to “GOES-MODIS FRE”. It was used to calculate grid-level biomass-burning emissions, which is referred as to “GOES-MODIS BBE”, using the following equation:

$$BBE_{FRE} = \sum_{i=1}^{p}\left(BC_i \times EF_i\right) = \sum_{i=1}^{p}\left(\beta \times FRE_i \times EF_i\right) \quad (7)$$

where BBE_{FRE} is total hourly emissions (kg) for a grid cell, BC_i and EF_i are hourly biomass consumption (kg) and PM2.5 or CO emissions factor for the ith ecosystem (a total of p ecosystems that is the same as equation (6)) in a grid cell, respectively. The emission factor was adopted from the GFED4 (Table 2) (van der Werf et al., 2017) that were compiled based on (Akagi et al., 2011; Andreae and Merlet, 2001). This is to reduce the emission-factor-caused difference in comparison with existing inventories in section 2.7.2, although emission factor could vary significantly with combustion efficiency (Liu et al., 2017; Polivka et al., 2016). Because emission factor is only available for five land cover types (Table 2), the ecosystem specific emission factor in equation (7) was obtained by cross-walking GLCC classes to these land cover types. β is the FRE biomass combustion coefficients (FBCC, 0.368 kg MJ^{-1}) (Wooster et al., 2005), and FRE_i is hourly GOES-MODIS FRE in the ith ecosystem. Note that both PM2.5 and CO estimates present very similar temporal and spatial pattern because their only difference is emission factors, so that only PM2.5 estimates are presented in detail in the result section. The CO is only discussed in order to improve the evaluation of GOES-MODIS BBE estimates (c.f. Sections 2.7.3 and 3.5).

Table 2. Emission factors (units: g kg^{-1}) of PM2.5 and CO

Emission species	Forest	Savanna, Shrubs, grasslands	Croplands
PM2.5	12.9	7.17	6.26
CO	88.0	63.0	102.0

2.7. Evaluations of biomass-burning emissions

Because of the lack of ground truth emissions, GOES-MODIS BBE was evaluated by comparing with other datasets. These datasets were: (1) BBE modeled using Landsat burned area and fuel loadings, which was called Landsat BBE; (2) existing emissions inventories; (3) the hourly BBE simulated by a biogeochemical model.

2.7.1. Comparison of GOES-MODIS BBE with Landsat BBE

GOES-MODIS BBE was first evaluated by comparing with Landsat BBE using the simple ordinary least squares regression. The GOES-MODIS BBE was estimated from FRE biomass combustion coefficients and GOES-MODIS FRE using equation (7), and the Landsat BBE was calculated based on total burned area and fuel loading in a fire event as described in equation (8) (see the following two paragraphs). Because estimation of GOES-MODIS BBE and Landsat BBE applied the same emission factors, the evaluation of GOES-MODIS BBE was conducted by comparing GOES-MODIS FRE based biomass consumption (BC) with Landsat burned area based BC. Landsat BC was calculated in a set of burned areas. Specifically, a Landsat burned area (corresponding to a fire event) was selected if the MODIS and GOES active fire detections covered more than 95% of the burned area, which minimized the effect of missing detections from MODIS and GOES observations. As a result, a total of 129 qualified burned areas were extracted in 2011, 2013, 2014, and 2015, which were located in the western CONUS.

In a Landsat burned area, the BC was estimated using the conventional model (Seiler and Crutzen, 1980) as:

$$BC_{Landsat} = \sum_{t=1}^{n} \sum_{k=1}^{3} A_{t,k} M_{t,k} C_{t,k} \tag{8}$$

where $BC_{Landsat}$ is the total biomass consumption (kg), A is the Landsat burned area (km^2), M is FCCS (Fuel Characteristic Classification System) fuel loading (kg m^{-2}), C is the combustion completeness (unitless: 0-1), t is FCCS fuelbed category, n is the number of fuelbed categories, and k is MTBS burn severity class.

The three parameters in Equation (8) were calculated in the same way as Li et al (2018b). Specifically, the burned area A was calculated from three Landsat MTBS severity classes (low, moderate, and high). Fuel loading M was obtained from the FCCS 3.0 that provides a 30-m fuelbed map and an associated lookup table of fuel loadings (http://www.fs.fed.us/pnw/fera/fccs/maps.shtml) for the year 2008. The FCCS 3.0 has 250 fuelbeds, and each fuelbed is separated into one or up to 18 categories (Ottmar et al., 2006). The study used the burn-severity-specific combustion completeness values (Li et al., 2018b) that were obtained by summarizing the published values associated with burn severity (Campbell et al., 2007; Ghimire et al., 2012) because burn severity reflects the degree of above-ground organic matter consumption from fire and relates to changes in living and dead biomass (Eidenshink et al., 2007; Keeley, 2009).

2.7.2. Comparison of GOES-MODIS BBE with existing emissions inventories

The monthly and annual PM2.5 in GOES-MODIS BBE from 2011 to 2015 were compared to existing six global emission inventories (GFED4, GFASv1.0 and v1.2, QFEDv2.4r6, and FINNv1.5, FEERv1.0g1.2, and FLAMBE) and two regional inventories (WFEIS0.5, and NEI 2011&2014) across the CONUS (Table 3). Among these emission inventories, six of them are based on the bottom-up approaches, and two of them are based on top-down approaches. Bottom-up approach refers to the calculation of BBE using emissions factors (bottom-up derived) and biomass consumptions that are estimated from either burned areas and fuel loadings or FRE; whereas the top-down approach models BBE using FRE and the top-down coefficients that are derived from FRP and satellite observed Aerosol Optical Depth (AOD) (Ichoku and Ellison, 2014). Note that the GFAS product contains two different versions for the period of 2011-2015: GFASv1.0 is available from January 2011 to September 2014 and the GFASv1.2 with better quality control covers from October 2014 to December 2015.

Table 3. Six global and two United States emissions inventories.

Inventories	Scale & Resolution	Method	Source data	References & products sites
GFED4	Global $0.25^\circ \times 0.25^\circ$, monthly	bottom-up	Burned area (MCD64A1), Fuel loadings (biogeochemical modeled)	van der Werf et al., 2017 Giglio et al., 2013 http://www.falw.vu/~gwerf/GFED/GFED4/
GFASv1.0&1.2	Global $0.5^\circ \times 0.5^\circ$ & $0.1^\circ \times 0.1^\circ$, daily	bottom-up	MODIS FRP (MOD14/MYD14)	Kaiser et al., 2012 http://join.iek.fz-juelich.de/macc/access
FINNv1.5	Global 1 km, daily	bottom-up	Burned area (MOD14/MYD14, MCD12Q1), Fuel loadings (literatures)	Wiedinmyer et al., 2011 http://bai.acom.ucar.edu/Data/fire/
FLAMBE	Global 1-4 km, Hourly	bottom-up	Burned area (WF_ABBA GOES, MOD14/MYD14), Fuel loadings (literatures)	Reid et al., 2009 (personal communication)
QFED2.4r6	Global $0.25^\circ \times 0.3125^\circ$, daily	top-down	MODIS FRP (MOD14/MYD14)	Darmenov and Silva., 2015 ftp://ftp.nccs.nasa.gov/aerosol/emissions/QFED/v2.4r6/
FEERv1.0g1.2	Global $0.1^\circ \times 0.1^\circ$, daily	top-down	GFAS1.2 FRP flux, emissions coefficients	Ichoku and Ellison., 2014 http://feer.gsfc.nasa.gov/data/emissions/
WFEISv0.5	United States (CONUS & Alaska), annual	bottom-up	Burned area (MCD64A1) Fuel loadings (FCCS)	French et al., 2014 https://wfis.mtri.org/
NEI	United States (county & States), annual	bottom-up	Observations from ground facilities and satellites	https://www.epa.gov/air-emissions-inventories/

2.7.3. Comparison of GOES-MODIS BBE with model-simulated BBE

GOES-MODIS BBE was further evaluated using the model-simulated BBE in the Rim Fire. The Rim Fire is the third largest fire event in the California fire records. The model-simulated hourly BBE (CO emissions) was estimated by performing an inversion on available ground-based and airborne-based measurements, including CO, over the Rim Fire from 21 to 27 August 2013 using the Weather Research and Forecasting model coupled with Chemistry (WRF-Chem) (Saide et al., 2015). The airborne CO measurements were collected by the NASA DC-8 flights during eight hours from 26 (18:00 UTC) to 27 (02:00 UTC) August 2013 (Toon et al., 2016). This BBE dataset was obtained by personal communication. The model-simulated CO emissions were compared to GOES-MODIS BBE (CO) over the 4-km modeling domain on an hourly basis.

3. Results

3.1. Spatial distribution of PM2.5 emissions

Biomass burnings annually release on average 717 Gg PM2.5 emissions across the CONUS in the four years of 2011, 2013, 2014, and 2015 (Fig. 7). The PM2.5 emissions are spatially contributed by a mixture of fires in forests, shrubs, and grasses in the western CONUS (419 Gg or 58%), agriculture and forest fires in the southeastern CONUS (92 Gg or 13%), prairie grass fires in Kansas and Oklahoma states (37 Gg or 5%) in the central CONUS, and agriculture burnings in the Mississippi River Valley (45 Gg or 6%) in the central south CONUS. However, the PM2.5 emissions are very limited in the northeastern CONUS.

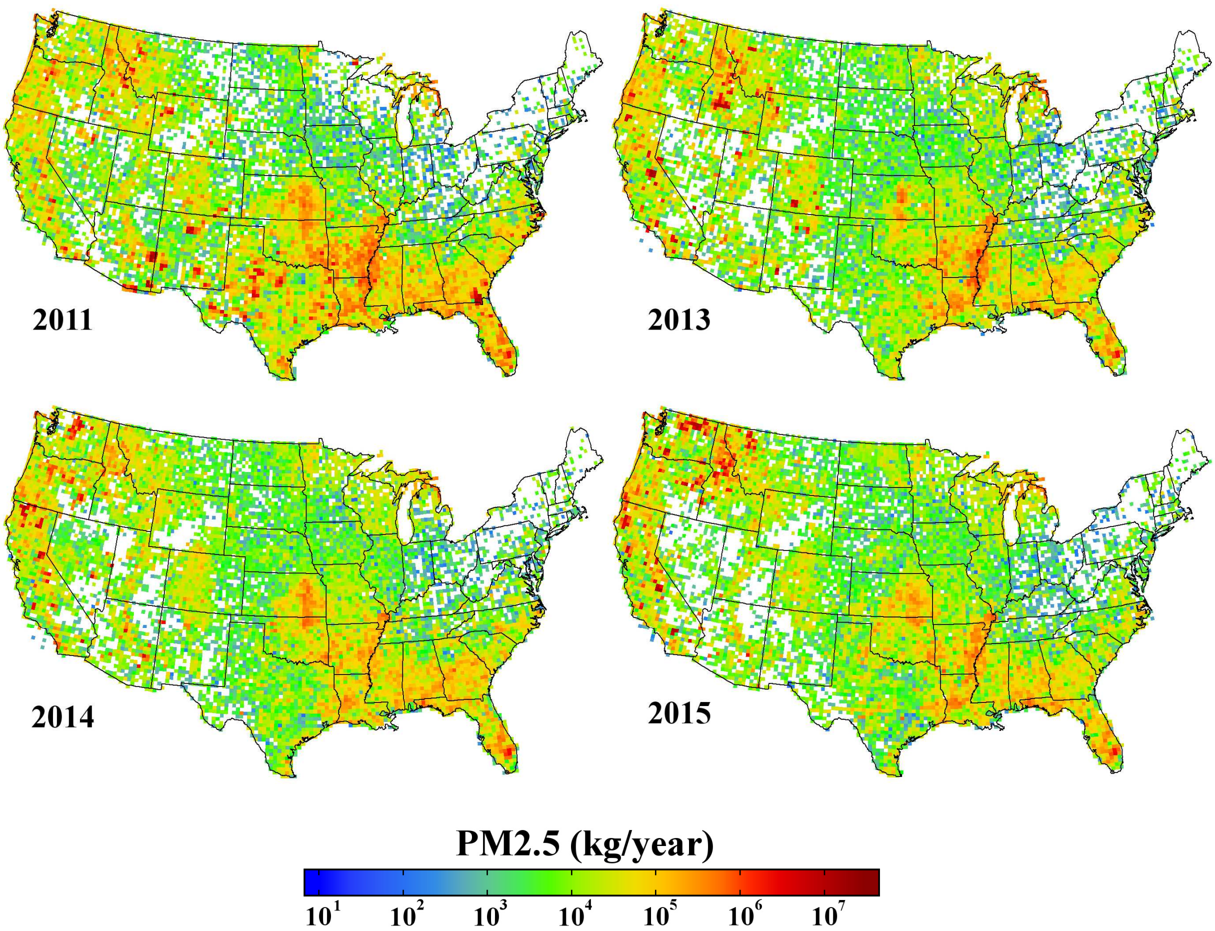

Fig. 7. Annual PM2.5 emissions at a 0.25°×0.3125° grid across the CONUS in four years of 2011, 2013, 2014, and 2015.

PM2.5 emissions vary greatly among CONUS states (Fig. 8). The high mean annual PM2.5 emission appears in five Pacific Northwest states: California (115 Gg), Idaho (58 Gg), Washington (54 Gg), Oregon (41 Gg), and Montana (34 Gg). The total PM2.5 emissions in these states and California alone accounts for 42% and 16% of the annual PM2.5 in the CONUS, respectively. They are followed by the PM2.5 emissions in three southwest states (Texas: 47 Gg, Arizona: 39 Gg, and New Mexico: 24 Gg), and three southeast states (Florida: 32 Gg, Arkansas: 29 Gg, and Georgia: 26 Gg). During the four years, the highest PM2.5 appears in 2015 and 2011, particularly in the Pacific Northwest states, and most southwest and southeast states.

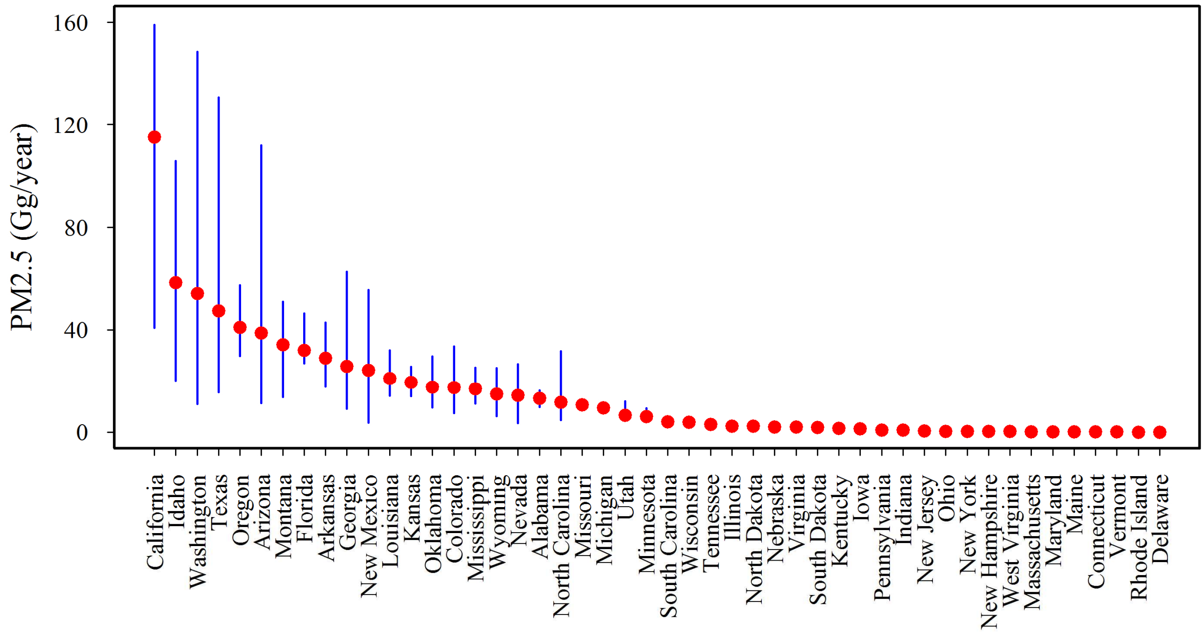

Fig. 8. Annual mean PM2.5 emissions in 48 states in four years of 2011, 2013, 2014, and 2015. The red dots represent annual mean PM2.5 emission and the vertical bars (in blue) show the maximum and minimum of annual PM2.5 emission in each state.

Annual PM2.5 emissions differ among land cover types (Fig. 9). The biomass burnings are on average 6% (42 Gg), 24% (174 Gg), and 70% (501 Gg) in the croplands, grasslands-shrublands-savannas, and forests, respectively.

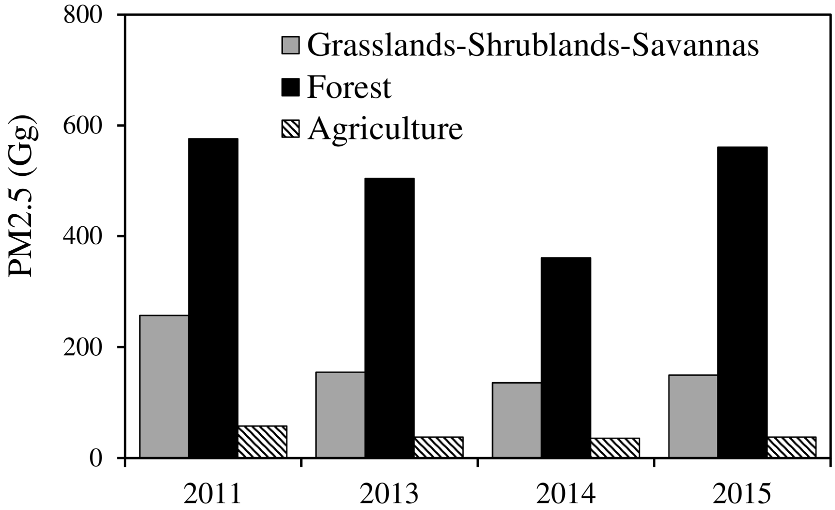

Fig. 9. Annual PM2.5 emissions in land cover types: croplands, forests, and grasslands-shrublands-savannas in four years of 2011, 2013, 2014, and 2015.

3.2. Temporal variation in the PM2.5 emissions

PM2.5 emissions display a strong diurnal variation across the CONUS (Fig. 10). The PM2.5 emissions with all ecosystems as a whole show a unimodal diurnal variation, which increases sharply at local time 9:00, reach the peak between 13:00 and 14:00, and then decrease until the midnight. The diurnal variations in forests, croplands, and savannas-shrublands-grasslands display a single peak approximately between 13:00 and 14:00. The PM2.5 estimates in daytime (6:00-18:00) differ considerably from the nighttime (18:00-6:00). Overall, the daytime PM2.5 emissions are 272% of the nighttime emissions but this discrepancy varies with ecosystem. The daytime emissions account for 81% in grasslands, savannas and shrublands, and 94% in croplands. In forests, approximately 90% and 10% of PM2.5 emissions are released during daytime and nighttime, respectively, in the eastern CONUS, whereas the nighttime burnings (especially from 18:00 to 24:00) in the western CONUS contribute 32% of PM2.5 emissions.

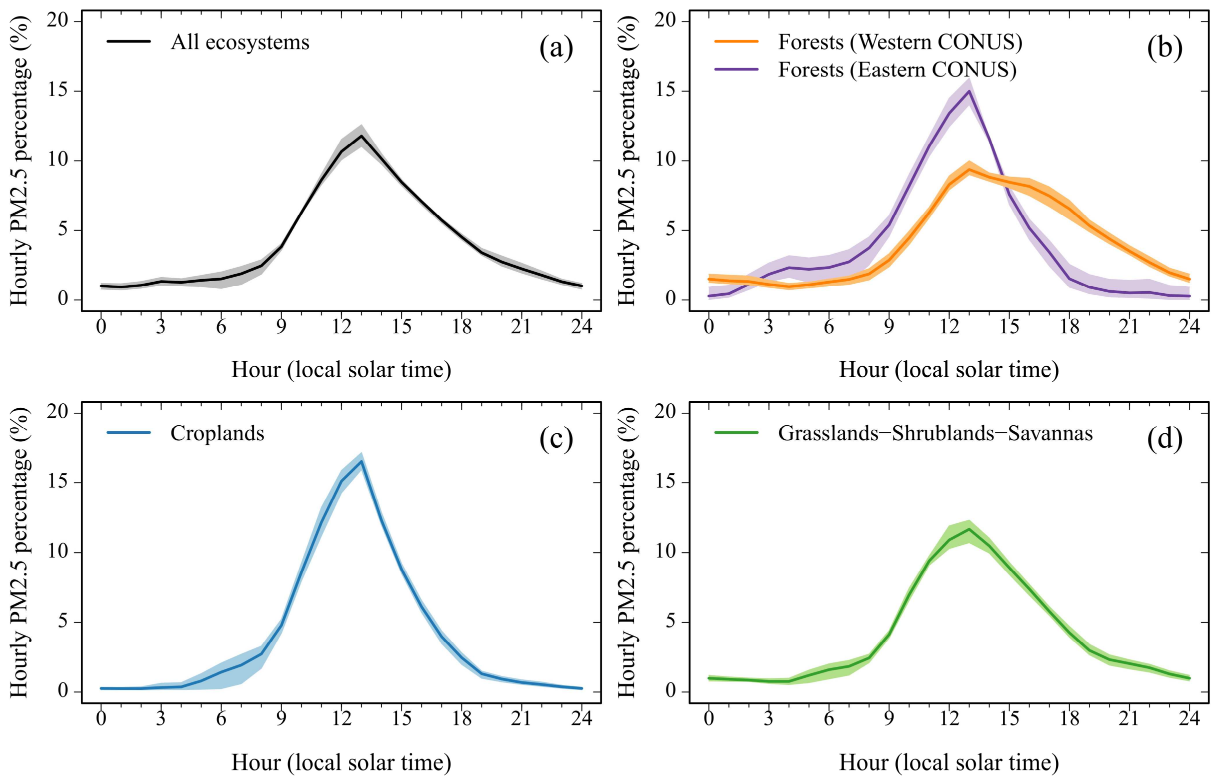

Fig. 10. Diurnal variation of PM2.5 emissions across the CONUS. The solid line is the four-year mean PM2.5 emissions in every hour, and the shading area represents inter-annual variation. (a) All ecosystems, (b) forests (forests were divided by 100°W longitude line into two groups: western and eastern CONUS because of the distinct difference in fire characteristics in two groups (Malamud et al., 2005)), (c) croplands, and (d) a combination of grasslands, shrublands, and savannas.

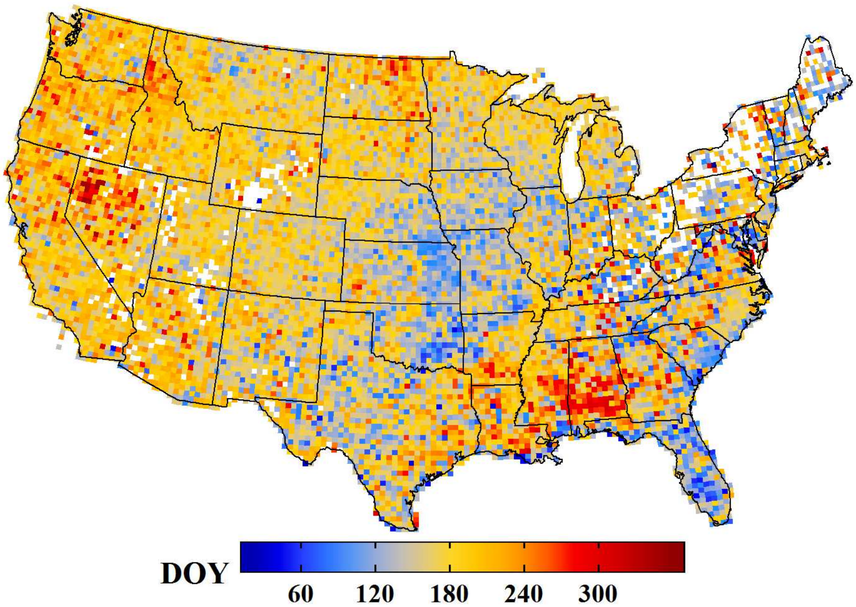

Fig. 11. Four-year mean seasonal peak time (day of year (DOY)) of the PM2.5 emissions at a 0.25°×0.3125° grid.

The peak time of seasonal PM2.5 emissions shows strong variations across the CONUS (Fig. 11). In the western CONUS, the emissions mainly reach peaks during July-September although the peak appears through winter and early spring months in a very small portion of areas. In the central CONUS, there are two main peak time periods: March to April in the middle central states (Kansas, Oklahoma, Missouri, Iowa, and Nebraska states), and July to September in other states. The peak time periods in the eastern CONUS are complex. Emissions reach the peak during the period from January to early April in most areas in Florida, August and September in the Mississippi river valley, and winter months in the south Mississippi and south Alabama.

3.3. Evaluation of biomass-burning emissions estimated from GOES-MODIS FRE

Total biomass consumption estimates calculated from the GOES-MODIS FRE (BC_{FRE}) are comparable with those estimated from 30m Landsat burned areas and FCCS fuel loadings ($BC_{Landsat}$) (Fig. 12). BC_{FRE} in the 129 selected fire events, which ranges from 0.03 - 5.7 Tg, is significantly correlated to $BC_{Landsat}$ (R^2=0.85, $p<0.001$) that ranges from 0.01 - 4.8 Tg. Overall, BC_{FRE} is relatively underestimated over some fires but overestimated in the other fires compared to $BC_{Landsat}$. Overall, BC_{FRE} is well comparable (~4% larger) with $BC_{Landsat}$.

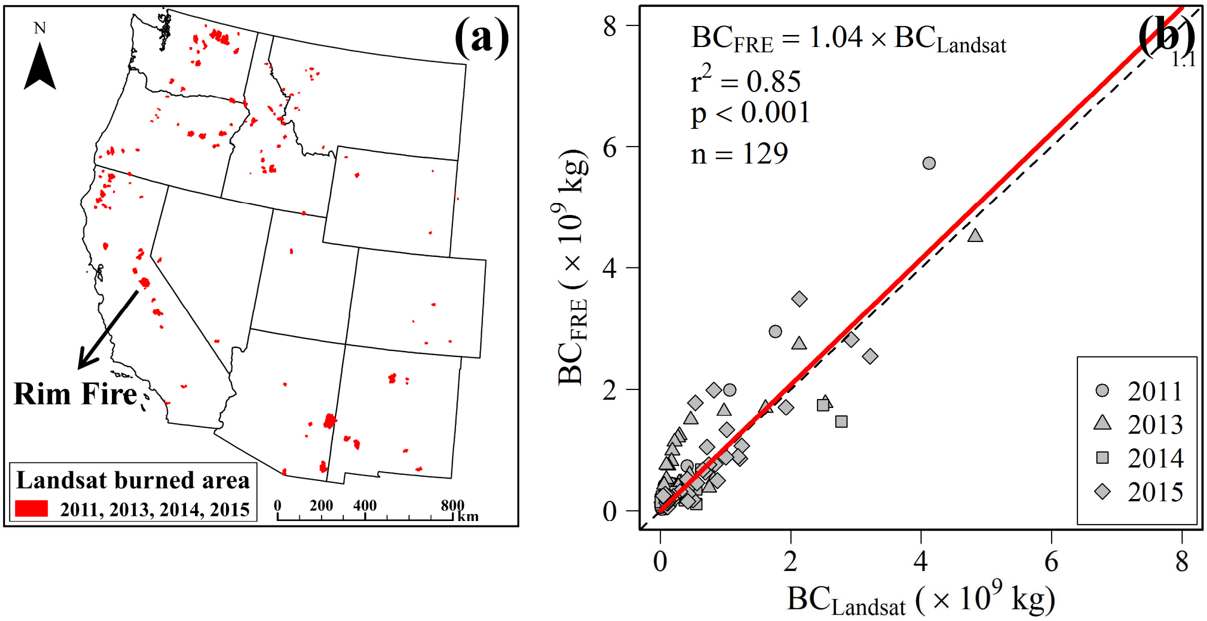

Fig. 12. Comparison between the GOES-MODIS-FRE based total biomass consumption (BC_{FRE}) and the Landsat-burned-area-based total biomass consumption ($BC_{Landsat}$) across the western CONUS. (a) Distribution of the 129 selected fire events from 2011 to 2015. (b) Scatterplot of BC_{FRE} against $BC_{Landsat}$.

The monthly GOES-MODIS PM2.5 reveals seasonal similarity and discrepancy with six global emission inventories (Fig. 13). The overall similarity is found that the emissions generally increase from January, reach the first peak in March or April, decrease in May, but climb up again rapidly and reach the second peak in August, and then decrease until the end of a year. However, differences are remarkable in an individual year among inventories. For instance, the highest peak in FEERv1.0g1.2 PM2.5 occurred in April in 2011 and 2014, which contrasts sharply with the GOES-MODIS PM2.5 and all other inventories. Moreover, FINNv1.5 PM2.5 does not show distinctive fire season as other inventories, especially in 2011, 2013, and 2014. Overall, the seasonal pattern in the GOES-MODIS PM2.5 estimates matches the best with FLAMBE.

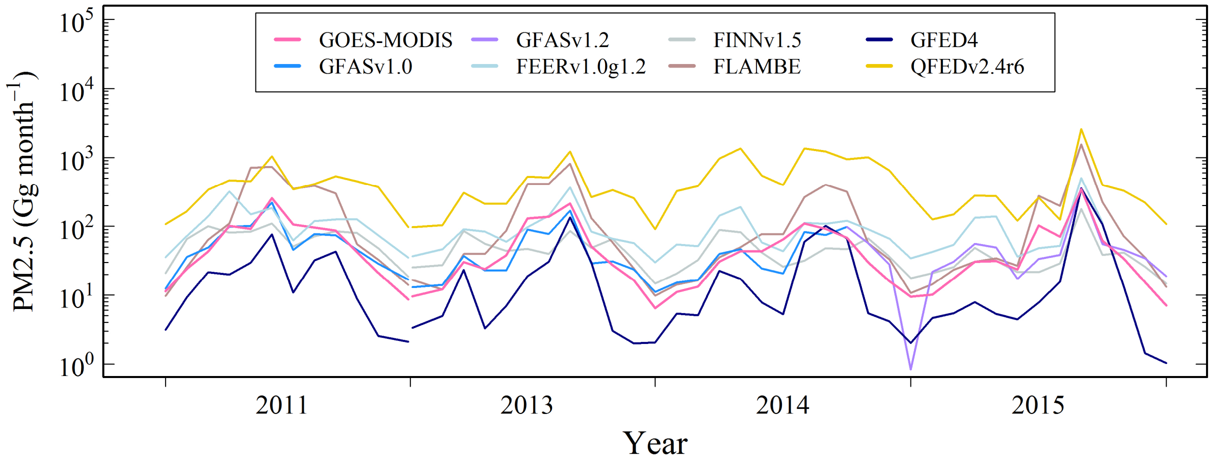

Fig. 13. Comparison of the monthly total GOES-MODIS PM2.5 emissions with other six inventories across the CONUS in four years of 2011, 2013, 2014, and 2015.

The average of monthly PM2.5 emissions in the four years varied largely among various BBE datasets (Table 4). The GOES-MODIS PM2.5 is similar to GFAS1.x and FINNv1.5 with a difference less than 12%. The GFED4 are the smallest among all BBE data sets, but comparable with the GOES-MODIS PM2.5 from October to following February (Fig. 13). In contrast, the FEERv1.0g1.2, FLAMBE, and QFEDv2.4r6 are approximately larger than the GOES-MODIS PM2.5 by a factor of 1, 2, and 7, respectively.

Table 4. The average of monthly PM2.5 emissions (Gg) of the GOES-MODIS and six inventories in four years of 2011, 2013, 2014, and 2015

GOES-MODIS	GFED4	FINNv1.5	GFASv1.x	FEERv1.0g1.2	FLAMBE	QFEDv2.4
59.7	28.2	50.5	55.3	100.2	181.6	485.6

The annual GOES-MODIS PM2.5 was also compared with two annual inventories of WFEISv0.5 in 2011 and 2013, and NEI in 2011 and 2014. The comparison shows that the annual GOES-MODIS PM2.5 is on average 37% larger than WFEISv0.5 in 2011 and 2013, but 54% smaller than NEI in 2011 and 2014.

The hourly CO estimates from the GOES-MODIS and the WRF-Chem model show overall similar temporal patterns in the 2013 Rim Fire, California, particularly when the model was constrained by both ground-based and airborne-based observations (Fig. 14). During the eight hours from 18:00 UTC (26 August) to 02:00 UTC (27 August) between two gray dashed lines when the WRF-Chem model was constrained by both the airborne-based and ground-based observations, the GOES-MODIS CO is almost the same as the model-simulated CO, with a difference of less than 1% on an hourly average. However, the discrepancy significantly increases during other periods when the model was constrained only by the ground-based observations. The GOES-MODIS CO on hourly average is 38% and 164% of the model-simulated CO during the daytime (14:00-24:00 UTC) and nighttime (1:00-13:00 UTC), respectively.

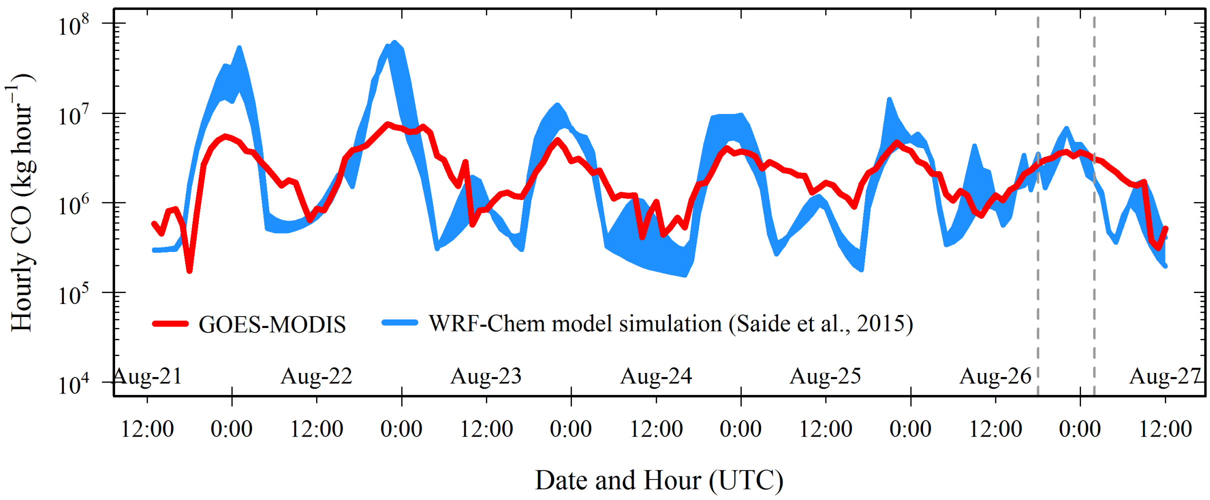

Fig. 14. Comparison of hourly CO emissions in the Rim Fire over the 4-km modeling domain. The red line is the GOES-MODIS CO estimates, and the light blue area represents the estimates simulated by the WRF-Chem model. CO simulation from WRF-Chem model was performed using both ground- and airborne-based observations during the time period within two gray dash lines (18:00 UTC on 26 to 02:00 UTC on 27 August) while only the ground observations during the rest time period.

4. Discussion

Satellite-based FRP offers a potential tool for improving the accuracy of BBE estimates in near real-time, which elevates the application capability of BBE in modeling air quality, and environmental and metrological conditions (Kaufman et al., 1998; Peterson and Wang, 2013; Peterson et al., 2014; Roberts and Wooster, 2008; Wooster, 2002; Wooster et al., 2005; Zhang et al., 2012). High-quality BBE could be calculated from diurnal FRP variations if FRP observations are available at a high spatiotemporal resolution. However, the existing solutions of FRP from either MODIS or geostationary satellites alone hardly produce BBE that satisfies models for forecasting air quality and environmental changes (Andela et al., 2015). By fusing the high temporal GOES FRP with high spatial MODIS FRP observations, this study reconstructed diurnal FRP cycles every 15 minutes to estimate hourly BBE at a 0.25°×0.3125° grid across the CONUS from 2011 to 2015.

This study indicates the importance of diurnal FRP cycles in the estimation of BBE. MODIS FRP has been commonly used to calculate daily mean FRP flux and thereafter estimate daily FRE and BBE (Darmenov and Silva, 2015; Kaiser et al., 2012), or directly related to BBE estimates (Ichoku and Ellison, 2014; Ichoku and Kaufman, 2005) by assuming that MODIS observations are able to capture the structure of diurnal fire activities. However, MODIS FRE and BBE could contain high uncertainties because of the long temporal gaps between any two valid observations. Although there are as many as four observations during a day, MODIS FRP retrievals are not available for the fires with the obscuration of clouds, thick smoke plumes, or tree canopies. This is particularly the case for the short-life agriculture burnings and fires occur in cloud-frequent-covered southeastern CONUS. Although the MODIS diurnal FRP cycle could be established by assuming that FRP follows a Gaussian-shaped diurnal model (Andela et al., 2015; Ellicott et al., 2009; Konovalov et al., 2014; Vermote et al., 2009), the GOES FRP demonstrates that the diurnal FRP cycle varies with ecosystems rather than presenting a simple uniform shape (Fig. 4). Furthermore, as hourly PM2.5 from GOES-MODIS FRP suggests that diurnal profile of PM2.5 in western CONUS forests is asymmetric, where fire activity during evening contributes a significant portion of daily PM2.5 (Fig. 10b). On the other hand, fire duration could vary greatly in different season and ecosystems (Fig. 5 and 6), which is able to be determined from GOES but not from MODIS observations. Consequently, it is critical to reconstruct diurnal FRP cycles and fire duration from geostationary satellites for accurately calculating FRE and BBE.

This study also reveals the difference in spatiotemporal patterns of emissions from wildfires and agriculture burnings across the CONUS. The major sources of wildfires emissions vary spatially in the western CONUS interannually (Fig. 7). In California, for example, the annual PM2.5 has increased by approximately 300% from 2011 - 2015 (Fig. 7), which is most likely related to the exceptional drought underwent in the same periods (Asner et al., 2016; Griffin and Anchukaitis, 2014; Robeson, 2015). The big drought occurred in 2011 in the southwest CONUS (Texas, Arizona, and New Mexico) elevated PM2.5 emissions by 530% that accounted for 30% (298 Gg) of the annual PM2.5 in the CONUS (Fig. 7) (Nielsen-Gammon, 2011). In contrast, the agriculture burnings (the Mississippi River Valley and the Florida Everglades) burn annually with very small inter-annual variation in PM2.5 emissions (Fig. 7), which is similar to the small interannual variation in cropland burned areas across the CONUS (McCarty et al., 2009; Randerson et al., 2012; Zhang and Kondragunta, 2008). Moreover, the average diurnal variation of PM2.5 demonstrates that the major emissions from agriculture burning mainly released from 9:00 to 18:00 local solar time (Fig. 10c), which is most likely related to timings of agriculture burning practices (Brenner and Wade, 2003; Kim Oanh et al., 2011; McRae et al., 1994). However, wildfires can burn during nighttime and contribute a significant portion of emissions compared to daytime emissions (Fig. 10b).

The GOES-MODIS BBE estimates are overall comparable with the Landsat based BBE estimates over the selected 129 fires although their difference could be considerable in some individual fire events. The discrepancy could be attributed to uncertainties of parameterization in the two different BBE estimating methods. For the Landsat based BBE (equation (8)), parameters of the FCCS fuel loading and combustion completeness likely contain considerable uncertainty. The FCCS fuel loading is static, which does not reflect seasonal and interannual variations associated with variation of fuel moisture and changes of fuel bed (Pellizzaro et al., 2007). Combustion completeness was summarized from a large number of published sources across the CONUS (Li et al., 2018b), which may not adequately represent the variation in fire behavior and fuel moisture (Hély et al., 2003). On the other hand, the uncertainty in GOES-MODIS BBE could be raised from the calculation of satellite FRP and the reconstruction of FRP diurnal cycle. Although MODIS and GOES FRP was adjusted to reduce the view angle effects and GOES FRP was further calibrated against MODIS FRP, MODIS and GOES FRP could be affected by other factors, including attenuation of tree canopy (Roberts et al., 2018) and effect of sub-pixel features on FRP retrieval (Peterson et al., 2013; Peterson & Wang, 2013). Nevertheless, for the 2013 Rim Fire in California, both the GOES-MODIS based biomass consumption (4.5 Tg) and the Landsat based estimate (4.8 Tg) are similar to the Lidar-and-Landsat based estimates of biomass consumption (3.93 - 6.58 Tg) in (Garcia et al., 2017).

Although comparisons show similarities and discrepancies among BBE inventories, the novelty of algorithm developed in this study is to calculate the GOES-MODIS emissions by improving diurnal FRP and FRE quantification while most other methods focus on tuning the coefficients or scaling factors to convert FRP to fire emissions. Generally, the emissions from the top-down-approach-based QFEDv2.4r6 and FEERv1.0g1.2 are larger than those from the bottom-up-approach-based estimates by a factor of 1-7, which has also been found in regional (Zhang et al., 2014) and global emissions estimates (Ichoku and Ellison, 2014; Kaiser et al., 2012; Zhang et al., 2012). It is likely due to the fact that both the QFED and FEER use large coefficients (converting FRP to emissions) that are adjusted using AOD observations for atmospheric models (Darmenov and Silva, 2015; Ichoku and Ellison, 2014). Moreover, the FEER emissions show the highest peaks during spring months in the years 2011 and 2014 while other inventories reveal the highest peaks in summer months (Fig. 13). During spring months, majority of fires occur in central and southeastern CONUS (Fig. 11) where the smoke plumes have not been well studied (Val Martin et al., 2010). This is likely associated with the abnormal peaks in FEER emissions because smoke plume injection height is critical in deriving the FEER emissions coefficients (Ichoku and Ellison, 2014). Although the GOES-MODIS PM2.5 is quantitatively comparable with GFASv1.x (Table 4), the mean annual total FRE of GOES-MODIS is 152% of FRE estimated from GFASv1.x (this result did not show here). This discrepancy in FRE is most likely offset by the much larger biomass combustion factors used in GFASv1.x (Kaiser et al., 2012). The GOES-MODIS PM2.5 is also numerically similar to FINNv1.5 (Table 4) but FINNv1.5 emissions estimates are highly uncertain due to several uncertainty sources, especially the burned area that is simply estimated from MODIS active fire counts (Wiedinmyer et al., 2011). Among all bottom-up-approach-based inventories, the FLAMBE is larger than others by a factor of 2-4 (Table 4), which is similar to the previous finding obtained by comparing FLAMBE with GFED across the CONUS (Reid et al., 2009). The FLAMBE emission estimates could be overestimated in large fires in the western CONUS because large fires (or fire clusters) greatly boost up FLAMBE emissions in Northern Africa (Zhang et al., 2014). Nevertheless, the seasonal variation of the GOES-MODIS matches the best with FLAMBE (Fig. 13), which is likely attributed to the use of GOES WF_ABBA data in both approaches. In contrast, GFED4 is the smallest (less by a factor of 1-4 than others), which could be related to the underestimates of MODIS burned areas (Randerson et al., 2012). The NEI is larger than all other bottom-up-approach-based inventories (except FLAMBE) by a factor of 2-3, which may suggest that the ground-based observations include many more fires than satellites detected fires (Short, 2015). However, the NEI only produces annual emissions calculated from fuel loadings and burned area reported from federal, state, and local agencies, which is lack of validations. To sum up, the differences in either models of emissions estimation or the methods of parameterization can result in significant discrepancy among inventories.

The 15-minute diurnal FRP cycles reconstructed from the fused GOES and MODIS FRP have several advantages. First, FRP in small fires (10-30 MW) that are missed by GOES (Roberts and Wooster, 2008; Xu et al., 2010) are compensated by calibrating GOES FRP against MODIS FRP. Second, the reconstructed diurnal FRP cycles partially mitigate the underestimation of FRE due to omission errors in FRP retrievals from GOES and MODIS that are attributed to the dynamic transitions of combustion phases and obscurations of clouds. During transitions of combustion phase, a fire is detectable from GOES or MODIS when it burns intensely in favorable conditions while it is omitted when it is cooling down and smoldering (Giglio et al., 2003; Wooster et al., 2003). Third, the reconstructed diurnal FRP cycles may well represent diurnal variations of fires in certain ecosystems. This was demonstrated by the good agreement of hourly CO emissions between the GOES-MODIS estimates and the WRF-Chem model simulation in the Rim Fire. It is particularly true compared to the WRF-Chem simulation that is constrained by both ground- and airborne-based measurements during 26 - 27 August 2013 (Fig. 14).

The fused FRP from MODIS and GOES retrievals and the reconstructed diurnal FRP cycles evidently enhance the capability of BBE estimates in near real-time; however, some uncertainties could still remain as the data processing is mostly empirical. However, the algorithm developed in this study is expected to reconstruct more accurate diurnal FRP cycles and improve BEE estimates by fusing FRP from new polar-orbiting and geostationary satellites in future. The Visible Infrared Imaging Radiometer Suite (VIIRS) onboard the Suomi National Polar-Orbiting Partnership (NPP) satellite and the Joint Polar Satellite System (JPSS) series is producing FRP at a spatial resolution of 750 m (at nadir), which can capture much smaller fires than MODIS does (Csiszar et al., 2014). On the other hand, the Advanced Baseline Imager (ABI) onboard GOES-R is to retrieve FRP at a spatial resolution of 2 km (at nadir) every 5 minutes (Schmidt et al., 2012), which is significantly improved relative to FRP from current GOES Imager.

5. Conclusions

We reconstructed ecosystem-specific diurnal FRP cycles by fusing high temporal resolution GOES FRP with high spatial resolution MODIS FRP to estimate BBE across the CONUS. The reliable diurnal FRP cycles are essential to accurately calculate FRE that plays a key role in BBE estimation from both bottom-up and top-down models. While the estimation of BBE using limited daily observations of polar-orbiting satellites raises considerable uncertainties, the hourly GOES-MODIS BBE can be effectively estimated from diurnal FRP cycles in a $0.25°\times0.3125°$ grid, which could provide reliable inputs for modeling smoke transportation (Wang et al., 2006) and quantifying the BBE impact on air quality in near real-time (Wang et al., 2018a). The derived hourly BBE profiles based on reconstructed diurnal FRP cycles (Fig. 10) help to redistribute daily (or longer temporal resolution) BBE inventories (e.g., QFED and GFED) to an hourly scale for near real-time applications and modeling simulations as well. Further, the GOES-MODIS BBE is comparable with the estimates using burned areas and fuel loadings in Landsat burned areas (~4% difference), and hourly emissions simulated using the WRF-Chem model (the best agreement with a difference < 1%). Moreover, the seasonal variation in GOES-MODIS BBE also shows good agreement with existing inventories and the magnitude differs from existing inventories by a factor of less than seven, which is smaller than the difference of a factor of ~10 in Northern Africa as found in Zhang et al. (2014).

Finally, the algorithm developed in this study provides a protocol to fuse FRP retrieved from the VIIRS and GOES-R ABI sensors. In this way, the diurnal FRP cycle with much higher temporal and spatial resolutions could be reconstructed and the BBE estimates could be greatly improved.

Acknowledgements

This research was funded by NOAA contracts NA14NES4320003 and BG-133E-15-SE-1613. The authors thank Dr. Pablo E. Saide for sharing the WRF-Chem model simulated CO emissions data in California Rim fire, and Dr. Edward J. Hyer and Dr. Luke T. Ellison for providing and discussing in uses of FLAMBE and FEER emissions inventories. The authors also want to thank all groups who contribute and make emissions inventories in Table 3 available to the public. The MODIS and GOES active fire data used in this study are available from NASA Level-1 and Atmosphere Archive & Distribution System (LAADS) (https://ladsweb.modaps.eosdis.nasa.gov/) and at NOAA (http://satepsanone.nesdis. noaa.gov/pub/FIRE/forPo/), respectively. The authors also thank two anonymous reviewers for their constructive comments that significantly improved this manuscript. The manuscript contents are solely the opinions of the author(s) and do not constitute a statement of policy, decision, or position on behalf of NOAA or the U. S. Government.

References

Akagi, S.K., Yokelson, R.J., Wiedinmyer, C., Alvarado, M.J., Reid, J.S., Karl, T., Crounse, J.D., Wennberg, P.O., 2011. Emission factors for open and domestic biomass burning for use in atmospheric models. Atmos. Chem. Phys. 11, 4039-4072, doi:https://doi.org/10.5194/acp-11-4039-2011.

Akimoto, H., 2003. Global Air Quality and Pollution. Science 302, 1716-1719, doi:https://doi.org/10.1126/science.1092666.

Andela, N., Kaiser, J.W., van der Werf, G.R., Wooster, M.J., 2015. New fire diurnal cycle characterizations to improve fire radiative energy assessments made from MODIS observations. Atmos. Chem. Phys. 15, 8831-8846, doi:https://doi.org/10.5194/acp-15-8831-2015.

Andreae, M.O., Merlet, P., 2001. Emission of trace gases and aerosols from biomass burning. Global Biogeochemical Cycles 15, 955-966, doi:https://doi.org/10.1029/2000GB001382.

Asner, G.P., Brodrick, P.G., Anderson, C.B., Vaughn, N., Knapp, D.E., Martin, R.E., 2016. Progressive forest canopy water loss during the 2012–2015 California drought. Proceedings of the National Academy of Sciences 113, E249-E255, doi:https://doi.org/10.1073/pnas.1523397113.

Bey, I., Jacob, D.J., Yantosca, R.M., Logan, J.A., Field, B.D., Fiore, A.M., Li, Q., Liu, H.Y., Mickley, L.J., Schultz, M.G., 2001. Global modeling of tropospheric chemistry with assimilated meteorology: Model description and evaluation. Journal of Geophysical Research: Atmospheres 106, 23073-23095, doi:https://doi.org/10.1029/2001JD000807.

Boden, T.A., Marland, G., Andres, R.J., 2017. Global, Regional, and National Fossil-Fuel CO2 Emissions, in: Carbon Dioxide Information Analysis Center, O.R.N.L., U.S. Department of Energy (Ed.), Oak Ridge, Tenn., U.S.A, doi:https://doi.org/10.3334/CDIAC/00001_V2017.

Bond, T.C., Doherty, S.J., Fahey, D.W., Forster, P.M., Berntsen, T., DeAngelo, B.J., Flanner, M.G., Ghan, S., Kärcher, B., Koch, D., Kinne, S., Kondo, Y., Quinn, P.K., Sarofim, M.C., Schultz, M.G., Schulz, M., Venkataraman, C., Zhang, H., Zhang, S., Bellouin, N., Guttikunda, S.K., Hopke, P.K., Jacobson, M.Z., Kaiser, J.W., Klimont, Z., Lohmann, U., Schwarz, J.P., Shindell, D., Storelvmo, T., Warren, S.G., Zender, C.S., 2013. Bounding the role of black carbon in the climate system: A scientific assessment. Journal of Geophysical Research: Atmospheres 118, 5380-5552, doi:https://doi.org/10.1002/jgrd.50171.

Boschetti, L., Eva, H.D., Brivio, P.A., Grégoire, J.M., 2004. Lessons to be learned from the comparison of three satellite-derived biomass burning products. Geophysical Research Letters 31, L21501, doi:https://doi.org/10.1029/2008JD011645.

Boschetti, L., Roy, D.P., 2009. Strategies for the fusion of satellite fire radiative power with burned area data for fire radiative energy derivation. Journal of Geophysical Research: Atmospheres 114, D20302, L21501, doi:https://doi.org/10.1029/2004GL021229.

Bowman, D.M.J.S., Balch, J.K., Artaxo, P., Bond, W.J., Carlson, J.M., Cochrane, M.A., D'Antonio, C.M., DeFries, R.S., Doyle, J.C., Harrison, S.P., Johnston, F.H., Keeley, J.E., Krawchuk, M.A., Kull, C.A., Marston, J.B., Moritz, M.A., Prentice, I.C., Roos, C.I., Scott, A.C., Swetnam, T.W., van der Werf, G.R., Pyne, S.J., 2009. Fire in the Earth System. Science 324, 481-484, doi:https://doi.org/10.1126/science.1163886.

Brenner, J., Wade, D., 2003. Florida's revised prescribed fire law: protection for responsible burners. No. 13, Tall Timbers Research Station, Tallahassee, FL, pp. 132-136.

Brown, J.F., Loveland, T.R., Ohlen, D.O., Zhu, Z.-L., 1999. The global land-cover characteristics database: the users' perspective. Photogrammetric Engineering and Remote Sensing 65, 1069-1074.

Campbell, J., Donato, D., Azuma, D., Law, B., 2007. Pyrogenic carbon emission from a large wildfire in Oregon, United States. Journal of Geophysical Research: Biogeosciences 112, G04014, doi:https://doi.org/10.1029/2007JG000451.

Crutzen, P.J., Andreae, M.O., 1990. Biomass Burning in the Tropics: Impact on Atmospheric Chemistry and Biogeochemical Cycles. Science 250, 1669-1678, doi:https://doi.org/10.1126/science.250.4988.1669.

Csiszar, I., Schroeder, W., Giglio, L., Ellicott, E., Vadrevu, K.P., Justice, C.O., Wind, B., 2014. Active fires from the Suomi NPP Visible Infrared Imaging Radiometer Suite: Product status and first evaluation results. Journal of Geophysical Research: Atmospheres 119, 2013JD020453, doi:https://doi.org/10.1002/2013JD020453.

Darmenov, A.S., Silva, A.d., 2015. The Quick Fire Emissions Dataset (QFED): Documentation of versions 2.1, 2.2 and 2.4, in: Koster, R.D. (Ed.), Technical Report Series on Global Modeling and Data Assimilation. NASA, p. 212.

Eastham, S.D., Jacob, D.J., 2017. Limits on the ability of global Eulerian models to resolve intercontinental transport of chemical plumes. Atmos. Chem. Phys. 17, 2543-2553, doi:https://doi.org/10.5194/acp-17-2543-2017.

Eidenshink, J., B. Schwind, K. Brewer, Z. Zhu, B. Quayle, Howard, S., 2007. A project for monitoring trends in burn severity. Fire Ecology 3, 19, doi:https://doi.org/10.4996/fireecology.0301003.

Ellicott, E., Vermote, E., Giglio, L., Roberts, G., 2009. Estimating biomass consumed from fire using MODIS FRE. Geophysical Research Letters 36, L13401, doi:https://doi.org/10.1029/2009GL038581.

Freeborn, P.H., Wooster, M.J., Hao, W.M., Ryan, C.A., Nordgren, B.L., Baker, S.P., Ichoku, C., 2008. Relationships between energy release, fuel mass loss, and trace gas and aerosol emissions during laboratory biomass fires. Journal of Geophysical Research-Atmospheres 113, D01301, doi:https://doi.org/ 10.1029/2007jd008679.

Freeborn, P.H., Wooster, M.J., Roberts, G., 2011. Addressing the spatiotemporal sampling design of MODIS to provide estimates of the fire radiative energy emitted from Africa. Remote Sensing of Environment 115, 475-489, doi:https://doi.org/10.1016/j.rse.2010.09.017.

Freeborn, P.H., Wooster, M.J., Roberts, G., Malamud, B.D., Xu, W., 2009. Development of a virtual active fire product for Africa through a synthesis of geostationary and polar orbiting satellite data. Remote Sensing of Environment 113, 1700-1711, doi:https://doi.org/10.1016/j.rse.2009.03.013.

Freeborn, P.H., Wooster, M.J., Roy, D.P., Cochrane, M.A., 2014. Quantification of MODIS fire radiative power (FRP) measurement uncertainty for use in satellite-based active fire characterization and biomass burning estimation. Geophysical Research Letters 41, 2013GL059086, doi:https://doi.org/10.1002/2013GL059086.

French, N.H.F., de Groot, W.J., Jenkins, L.K., Rogers, B.M., Alvarado, E., Amiro, B., de Jong, B., Goetz, S., Hoy, E., Hyer, E., Keane, R., Law, B.E., McKenzie, D., McNulty, S.G., Ottmar, R., Pérez-Salicrup, D.R., Randerson, J., Robertson, K.M., Turetsky, M., 2011. Model comparisons for estimating carbon emissions from North American wildland fire. Journal of Geophysical Research: Biogeosciences 116, G00K05, doi:https://doi.org/10.1029/2010JG001469.

Garcia, M., Saatchi, S., Casas, A., Koltunov, A., Ustin, S., Ramirez, C., Garcia-Gutierrez, J., Balzter, H., 2017. Quantifying biomass consumption and carbon release from the California Rim fire by integrating airborne LiDAR and Landsat OLI data. Journal of Geophysical Research: Biogeosciences 122, 340-353, doi:https://doi.org/10.1002/2015JG003315.

Ge, C., Wang, J., Reid, J.S., 2014. Mesoscale modeling of smoke transport over the Southeast Asian Maritime Continent: coupling of smoke direct radiative effect below and above the low-level clouds. Atmos. Chem. Phys. 14, 159-174, doi:https://doi.org/10.5194/acp-14-159-2014.

Ghimire, B., Williams, C.A., Collatz, G.J., Vanderhoof, M., 2012. Fire-induced carbon emissions and regrowth uptake in western U.S. forests: Documenting variation across forest types, fire severity, and climate regions. Journal of Geophysical Research: Biogeosciences 117, G03036, doi:https://doi.org/10.1029/2011JG001935.

Giglio, L., 2007. Characterization of the tropical diurnal fire cycle using VIRS and MODIS observations. Remote Sensing of Environment 108, 407-421, doi:https://doi.org/10.1016/j.rse.2006.11.018.

Giglio, L., 2015. MODIS Collection 6 Active Fire Product User's Guide, https://cdn.earthdata.nasa.gov/conduit/upload/3865/MODIS_C6_Fire_User_Guide_A.pdf, last accessed on 11/08/2018.

Giglio, L., Boschetti, L., Roy, D.P., Humber, M.L., Justice, C.O., 2018. The Collection 6 MODIS burned area mapping algorithm and product. Remote Sensing of Environment 217, 72-85, doi:https://doi.org/10.1016/j.rse.2018.08.005.

Giglio, L., Csiszar, I., Justice, C.O., 2006. Global distribution and seasonality of active fires as observed with the Terra and Aqua Moderate Resolution Imaging Spectroradiometer (MODIS) sensors. Journal of Geophysical Research: Biogeosciences 111, G02016, doi:https://doi.org/10.1029/2005JG000142

Giglio, L., Descloitres, J., Justice, C.O., Kaufman, Y.J., 2003. An Enhanced Contextual Fire Detection Algorithm for MODIS. Remote Sensing of Environment 87, 273-282, doi:https://doi.org/10.1016/S0034-4257(03)00184-6.

Giglio, L., Randerson, J.T., van der Werf, G.R., 2013. Analysis of daily, monthly, and annual burned area using the fourth-generation global fire emissions database (GFED4). Journal of Geophysical Research: Biogeosciences 118, 317-328, doi:https://doi.org/10.1002/jgrg.20042.

Giglio, L., Schroeder, W., Justice, C.O., 2016. The collection 6 MODIS active fire detection algorithm and fire products. Remote Sensing of Environment 178, 31-41, doi:https://doi.org/10.1016/j.rse.2016.02.054.

Griffin, D., Anchukaitis, K.J., 2014. How unusual is the 2012–2014 California drought? Geophysical Research Letters 41, 9017-9023, doi:https://doi.org/10.1002/2014GL062433.

Hao, W.M., Liu, M.-H., Crutzen, P.J., 1990. Estimates of Annual and Regional Releases of CO2 and Other Trace Gases to the Atmosphere from Fires in the Tropics, Based on the FAO Statistics for the Period 1975–1980, in: Goldammer, J.G. (Ed.), Fire in the Tropical Biota: Ecosystem Processes and Global Challenges. Springer Berlin Heidelberg, Berlin, Heidelberg, pp. 440-462, doi:https://doi.org/10.1007/978-3-642-75395-4_20.

Hély, C., Alleaume, S., Swap, R.J., Shugart, amp, H., H., Justice, C.O., 2003. SAFARI-2000 characterization of fuels, fire behavior, combustion completeness, and emissions from experimental burns in infertile grass savannas in western Zambia. Journal of Arid Environments 54, 381-394, doi:https://doi.org/10.1006/jare.2002.1097.

Hudak, A.T., Dickinson, M.B., Bright, B.C., Kremens, R.L., Loudermilk, E.L., O'Brien, J.J., Hornsby, B.S., Ottmar, R.D., 2016. Measurements relating fire radiative energy density and surface fuel consumption – RxCADRE 2011 and 2012. International Journal of Wildland Fire 25, 25-37, doi:https://doi.org/ 10.1071/WF14159.

Ichoku, C., Ellison, L., 2014. Global top-down smoke-aerosol emissions estimation using satellite fire radiative power measurements. Atmos. Chem. Phys. 14, 6643-6667, doi:https://doi.org/10.5194/acp-14-6643-2014.

Ichoku, C., Kaufman, Y.J., 2005. A method to derive smoke emission rates from MODIS fire radiative energy measurements. Geoscience and Remote Sensing, IEEE Transactions on 43, 2636-2649, doi:https://doi.org/10.1109/TGRS.2005.857328.

Jacobson, M.Z., 2014. Effects of biomass burning on climate, accounting for heat and moisture fluxes, black and brown carbon, and cloud absorption effects. Journal of Geophysical Research: Atmospheres 119, 2014JD021861, doi:https://doi.org/10.1002/2014JD021861.

Johnston, F.H., Melody, S., Bowman, D.M.J.S., 2016. The pyrohealth transition: how combustion emissions have shaped health through human history. Philosophical Transactions of the Royal Society B: Biological Sciences 371, doi:https://doi.org/10.1098/rstb.2015.0173.

Justice, C.O., Giglio, L., Korontzi, S., Owens, J., Morisette, J.T., Roy, D., Descloitres, J., Alleaume, S., Petitcolin, F., Kaufman, Y., 2002. The MODIS fire products. Remote Sensing of Environment 83, 244-262, doi:https://doi.org/10.1016/S0034-4257(02)00076-7.

Kaiser, J.W., Heil, A., Andreae, M.O., Benedetti, A., Chubarova, N., Jones, L., Morcrette, J.J., Razinger, M., Schultz, M.G., Suttie, M., van der Werf, G.R., 2012. Biomass burning emissions estimated with a global fire assimilation system based on observed fire radiative power. Biogeosciences 9, 527-554, doi:https://doi.org/10.5194/bg-9-527-2012.

Kasischke, E.S., Loboda, T., Giglio, L., French, N.H.F., Hoy, E.E., de Jong, B., Riano, D., 2011. Quantifying burned area for North American forests: Implications for direct reduction of carbon stocks. Journal of Geophysical Research: Biogeosciences 116, G04003, doi:https://doi.org/10.1029/2011JG001707.

Kaufman, Y.J., Justice, C.O., Flynn, L.P., Kendall, J.D., Prins, E.M., Giglio, L., Ward, D.E., Menzel, W.P., Setzer, A.W., 1998. Potential global fire monitoring from EOS-MODIS. Journal of Geophysical Research: Atmospheres 103, 32215-32238, doi:https://doi.org/10.1029/98JD01644.

Kaufman, Y.J., Tanre, D., Boucher, O., 2002. A satellite view of aerosols in the climate system. Nature 419, 215-223, doi:https://doi.org/10.1038/nature01091.

Keeley, J.E., 2009. Fire intensity, fire severity and burn severity: a brief review and suggested usage. International Journal of Wildland Fire 18, 116-126, doi:https://doi.org/ 10.1071/WF07049.

Kim Oanh, N.T., Ly, B.T., Tipayarom, D., Manandhar, B.R., Prapat, P., Simpson, C.D., Sally Liu, L.J., 2011. Characterization of particulate matter emission from open burning of rice straw. Atmospheric Environment 45, 493-502, doi:https://doi.org/10.1016/j.atmosenv.2010.09.023.

Konovalov, I.B., Berezin, E.V., Ciais, P., Broquet, G., Beekmann, M., Hadji-Lazaro, J., Clerbaux, C., Andreae, M.O., Kaiser, J.W., Schulze, E.D., 2014. Constraining CO2 emissions from open biomass burning by satellite observations of co-emitted species: a method and its application to wildfires in Siberia. Atmos. Chem. Phys. 14, 10383-10410, doi:https://doi.org/10.5194/acp-14-10383-2014.

Kremens, R.L., Dickinson, M.B., Bova, A.S., 2012. Radiant flux density, energy density and fuel consumption in mixed-oak forest surface fires. International Journal of Wildland Fire 21, 722-730, doi:https://doi.org/10.1071/WF10143.

Kumar, S.S., Roy, D.P., Boschetti, L., Kremens, R., 2011. Exploiting the power law distribution properties of satellite fire radiative power retrievals: A method to estimate fire radiative energy and biomass burned from sparse satellite observations. Journal of Geophysical Research: Atmospheres 116, D19303, doi:https://doi.org/10.1029/2011JD015676.

Lelieveld, J., Evans, J.S., Fnais, M., Giannadaki, D., Pozzer, A., 2015. The contribution of outdoor air pollution sources to premature mortality on a global scale. Nature 525, 367-371, doi:https://doi.org/10.1038/nature15371.

Li, F., Zhang, X., Kondragunta, S., Csiszar, I., 2018a. Comparison of Fire Radiative Power Estimates From VIIRS and MODIS Observations. Journal of Geophysical Research: Atmospheres 123, 4545-4563, doi:https://doi.org/10.1029/2017JD027823.

Li, F., Zhang, X., Kondragunta, S., Roy, D.P., 2018b. Investigation of the Fire Radiative Energy Biomass Combustion Coefficient: A Comparison of Polar and Geostationary Satellite Retrievals Over the Conterminous United States. Journal of Geophysical Research: Biogeosciences 123, 722-739, doi:https://doi.org/10.1002/2017JG004279.

Liu, X., Huey, L.G., Yokelson, R.J., Selimovic, V., Simpson, I.J., Müller, M., Jimenez, J.L., Campuzano-Jost, P., Beyersdorf, A.J., Blake, D.R., Butterfield, Z., Choi, Y., Crounse, J.D., Day, D.A., Diskin, G.S., Dubey, M.K., Fortner, E., Hanisco, T.F., Hu, W., King, L.E., Kleinman, L., Meinardi, S., Mikoviny, T., Onasch, T.B., Palm, B.B., Peischl, J., Pollack, I.B., Ryerson, T.B., Sachse, G.W., Sedlacek, A.J., Shilling, J.E., Springston, S., St. Clair, J.M., Tanner, D.J., Teng, A.P., Wennberg, P.O., Wisthaler, A., Wolfe, G.M., 2017. Airborne measurements of western U.S. wildfire emissions: Comparison with prescribed burning and air quality implications. Journal of Geophysical Research: Atmospheres 122, 6108-6129, doi: https://doi.org/10.1002/2016JD026315.

Malamud, B.D., Millington, J.D.A., Perry, G.L.W., 2005. Characterizing wildfire regimes in the United States. Proceedings of the National Academy of Sciences of the United States of America 102, 4694-4699, doi:https://doi.org/10.1073/pnas.0500880102.

McCarty, J.L., Korontzi, S., Justice, C.O., Loboda, T., 2009. The spatial and temporal distribution of crop residue burning in the contiguous United States. Science of The Total Environment 407, 5701-5712, doi:https://doi.org/10.1016/j.scitotenv.2009.07.009.

McRae, D.J., Lynham, T.J., Frech, R.J., 1994. Understory prescribed burning in red pine and white pine. The Forestry Chronicle 70, 395-401, doi:https://doi.org/10.5558/tfc70395-4.

Mota, B., Wooster, M.J., 2018. A new top-down approach for directly estimating biomass burning emissions and fuel consumption rates and totals from geostationary satellite fire radiative power (FRP). Remote Sensing of Environment 206, 45-62, doi:https://doi.org/10.1016/j.rse.2017.12.016.

Mouillot, F., Schultz, M.G., Yue, C., Cadule, P., Tansey, K., Ciais, P., Chuvieco, E., 2014. Ten years of global burned area products from spaceborne remote sensing—A review: Analysis of user needs and recommendations for future developments. International Journal of Applied Earth Observation and Geoinformation 26, 64-79, doi:https://doi.org/10.1016/j.jag.2013.05.014.

Nielsen-Gammon, J., 2011. The 2011 Texas drought: a briefing packet for the Texas Legislature. https://senate.texas.gov/cmtes/82/c510/0110BI-JohnNielsen-Gammon.pdf, last accessed on 11/08/2018.

Ottmar, R.D., Prichard, S.J., Vihnanek, R.E., Sandberg, D.V., 2006. Modification and Validation of Fuel Consumption Models for Shrub and Forested lands in the Southwest, Pacific Northwest, Rockies, Midwest, Southeast and Alaska. Seattle Washington. https://www.firescience.gov/projects/98-1-9-06/project/98-1-9-06_final_report.pdf, last accessed on 11/08/2018.

Pausas, J.G., Ribeiro, E., 2013. The global fire–productivity relationship. Global Ecology and Biogeography 22, 728-736, doi:https://doi.org/10.1111/geb.12043.

Pellizzaro, G., Cesaraccio, C., Duce, P., Ventura, A., Zara, P., 2007. Relationships between seasonal patterns of live fuel moisture and meteorological drought indices for Mediterranean shrubland species. International Journal of Wildland Fire 16, 232-241, doi:https://doi.org/10.1071/WF06081.

Peterson, D., Hyer, E., Wang, J., 2014. Quantifying the potential for high-altitude smoke injection in the North American boreal forest using the standard MODIS fire products and subpixel-based methods. Journal of Geophysical Research: Atmospheres 119, 3401-3419, doi:https://doi.org/10.1002/2013JD021067.

Peterson, D., Wang, J., 2013. A sub-pixel-based calculation of fire radiative power from MODIS observations: 2. Sensitivity analysis and potential fire weather application. Remote Sensing of Environment 129, 231-249, doi:https://doi.org/10.1016/j.rse.2012.10.020.

Peterson, D., Wang, J., Ichoku, C., Hyer, E., Ambrosia, V., 2013. A sub-pixel-based calculation of fire radiative power from MODIS observations: 1: Algorithm development and initial assessment. Remote Sensing of Environment 129, 262-279, doi:https://doi.org/10.1016/j.rse.2012.10.036.

Polivka, T.N., Wang, J., Ellison, L.T., Hyer, E.J., Ichoku, C.M., 2016. Improving Nocturnal Fire Detection With the VIIRS Day–Night Band. IEEE Transactions on Geoscience and Remote Sensing 54, 5503-5519, doi:https:// doi.org/10.1109/TGRS.2016.2566665.

Randerson, J.T., Chen, Y., van der Werf, G.R., Rogers, B.M., Morton, D.C., 2012. Global burned area and biomass burning emissions from small fires. Journal of Geophysical Research: Biogeosciences 117, G04012, doi:https://doi.org/10.1029/2012JG002128.

Reid, J.S., Hyer, E.J., Prins, E.M., Westphal, D.L., Jianglong, Z., Jun, W., Christopher, S.A., Curtis, C.A., Schmidt, C.C., Eleuterio, D.P., Richardson, K.A., Hoffman, J.P., 2009. Global Monitoring and Forecasting of Biomass-Burning Smoke: Description of and Lessons From the Fire Locating and Modeling of Burning Emissions (FLAMBE) Program. Selected Topics in Applied Earth Observations and Remote Sensing, IEEE Journal of 2, 144-162, doi:https://doi.org/10.1109/JSTARS.2009.2027443.

Roberts, G., Wooster, M.J., Lagoudakis, E., 2009. Annual and diurnal african biomass burning temporal dynamics. Biogeosciences 6, 849-866, doi:https://doi.org/10.5194/bg-6-849-2009.

Roberts, G., Wooster, M.J., Lauret, N., Gastellu-Etchegorry, J.P., Lynham, T., McRae, D., 2018. Investigating the impact of overlying vegetation canopy structures on fire radiative power (FRP) retrieval through simulation and measurement. Remote Sensing of Environment 217, 158-171, doi:https://doi.org/10.1016/j.rse.2018.08.015.

Roberts, G.J., Wooster, M.J., 2008. Fire Detection and Fire Characterization Over Africa Using Meteosat SEVIRI. Geoscience and Remote Sensing, IEEE Transactions on 46, 1200-1218, doi:https://doi.org/10.1109/TGRS.2008.915751.

Robeson, S.M., 2015. Revisiting the recent California drought as an extreme value. Geophysical Research Letters 42, 6771-6779, doi:https://doi.org/10.1002/2015GL064593.

Saide, P.E., Peterson, D.A., da Silva, A., Anderson, B., Ziemba, L.D., Diskin, G., Sachse, G., Hair, J., Butler, C., Fenn, M., Jimenez, J.L., Campuzano-Jost, P., Perring, A.E., Schwarz, J.P., Markovic, M.Z., Russell, P., Redemann, J., Shinozuka, Y., Streets, D.G., Yan, F., Dibb, J., Yokelson, R., Toon, O.B., Hyer, E., Carmichael, G.R., 2015. Revealing important nocturnal and day-to-day variations in fire smoke emissions through a multiplatform inversion. Geophysical Research Letters 42, 2015GL063737, doi:https://doi.org/10.1002/2015GL063737.

Schmidt, C.C., Hoffman, J., Prins, E., Lindstrom, S., 2012. GOES-R Advanced Baseline Imager (ABI) Algorithm Theoretical Basis Document For Fire / Hot Spot Characterization V2.5. https://www.star.nesdis.noaa.gov/goesr/docs/ATBD/Fire.pdf, last access on 11/08/2018.

Schmidt, C.C., Prins, E.M., 2003. GOES wildfire ABBA applications in the western hemisphere, 2nd International Wildland Fire Ecology and Fire Management Congress and 5th Symp. on Fire and Forest Meteorology. Citeseer, pp. 16-20.

Schroeder, W., Csiszar, I., Giglio, L., Schmidt, C.C., 2010. On the use of fire radiative power, area, and temperature estimates to characterize biomass burning via moderate to coarse spatial resolution remote sensing data in the Brazilian Amazon. Journal of Geophysical Research: Atmospheres 115, doi:https://doi.org/10.1029/2009JD013769.

Seiler, W., Crutzen, P., 1980. Estimates of gross and net fluxes of carbon between the biosphere and the atmosphere from biomass burning. Climatic Change 2, 207-247, doi:https://doi.org/10.1007/BF00137988.

Short, K.C., 2015. Sources and implications of bias and uncertainty in a century of US wildfire activity data. International Journal of Wildland Fire 24, 883-891, doi:https://doi.org/10.1071/WF14190.

Toon, O.B., Maring, H., Dibb, J., Ferrare, R., Jacob, D.J., Jensen, E.J., Luo, Z.J., Mace, G.G., Pan, L.L., Pfister, L., Rosenlof, K.H., Redemann, J., Reid, J.S., Singh, H.B., Thompson, A.M., Yokelson, R., Minnis, P., Chen, G., Jucks, K.W., Pszenny, A., 2016. Planning, implementation, and scientific goals of the Studies of Emissions and Atmospheric Composition, Clouds and Climate Coupling by Regional Surveys (SEAC4RS) field mission. Journal of Geophysical Research: Atmospheres 121, 2015JD024297, doi:https://doi.org/10.1002/2015JD024297.

Val Martin, M., Logan, J.A., Kahn, R.A., Leung, F.Y., Nelson, D.L., Diner, D.J., 2010. Smoke injection heights from fires in North America: analysis of 5 years of satellite observations. Atmos. Chem. Phys. 10, 1491-1510, doi: https://doi.org/10.5194/acp-10-1491-2010.

van der Werf, G.R., Randerson, J.T., Giglio, L., van Leeuwen, T.T., Chen, Y., Rogers, B.M., Mu, M., van Marle, M.J.E., Morton, D.C., Collatz, G.J., Yokelson, R.J., Kasibhatla, P.S., 2017. Global fire emissions estimates during 1997–2016. Earth Syst. Sci. Data 9, 697-720, doi:https://doi.org/10.5194/essd-9-697-2017.

Venables, W.N., Ripley, B.D., 2002. Modern applied statistics with S, Fourth ed. Springer Science & Business Media.

Vermote, E., Ellicott, E., Dubovik, O., Lapyonok, T., Chin, M., Giglio, L., Roberts, G.J., 2009. An approach to estimate global biomass burning emissions of organic and black carbon from MODIS fire radiative power. Journal of Geophysical Research: Atmospheres 114, D18205, doi:https://doi.org/10.1029/2008JD011188.

Wang, J., Bhattacharjee, P.S., Tallapragada, V., Lu, C.H., Kondragunta, S., da Silva, A., Zhang, X., Chen, S.P., Wei, S.W., Darmenov, A.S., McQueen, J., Lee, P., Koner, P., Harris, A., 2018a. The implementation of NEMS GFS Aerosol Component (NGAC) Version 2.0 for global multispecies forecasting at NOAA/NCEP – Part 1: Model descriptions. Geosci. Model Dev. 11, 2315-2332, doi:https://doi.org/10.5194/gmd-11-2315-2018.

Wang, J., Christopher, S.A., Nair, U.S., Reid, J.S., Prins, E.M., Szykman, J., Hand, J.L., 2006. Mesoscale modeling of Central American smoke transport to the United States: 1. "Top-down" assessment of emission strength and diurnal variation impacts. Journal of Geophysical Research: Atmospheres 111, doi:https://doi.org/10.1029/2005jd006416.

Wang, J., van den Heever, S.C., Reid, J.S., 2009. A conceptual model for the link between Central American biomass burning aerosols and severe weather over the south central United States. Environmental Research Letters 4, 015003, doi:https://doi.org/10.1088/1748-9326/4/1/015003.

Wang, J., Yue, Y., Wang, Y., Ichoku, C., Ellison, L., Zeng, J., 2018b. Mitigating Satellite-Based Fire Sampling Limitations in Deriving Biomass Burning Emission Rates: Application to WRF-Chem Model Over the Northern sub-Saharan African Region. Journal of Geophysical Research: Atmospheres 123, 507-528, doi:https://doi.org/10.1002/2017JD026840.

Wiedinmyer, C., Akagi, S.K., Yokelson, R.J., Emmons, L.K., Al-Saadi, J.A., Orlando, J.J., Soja, A.J., 2011. The Fire INventory from NCAR (FINN): a high resolution global model to estimate the emissions from open burning. Geosci. Model Dev. 4, 625-641, doi:https://doi.org/10.5194/gmd-4-625-2011.

Wolfe, R.E., Nishihama, M., Fleig, A.J., Kuyper, J.A., Roy, D.P., Storey, J.C., Patt, F.S., 2002. Achieving sub-pixel geolocation accuracy in support of MODIS land science. Remote Sensing of Environment 83, 31-49, doi:https://doi.org/10.1016/S0034-4257(02)00085-8.

Wolfe, R.E., Roy, D.P., Vermote, E., 1998. MODIS land data storage, gridding, and compositing methodology: Level 2 grid. Geoscience and Remote Sensing, IEEE Transactions on 36, 1324-1338, doi:https://doi.org/10.1109/36.701082.

Wooster, M.J., Roberts, G., Perry, G.L.W., Kaufman, Y.J., 2005. Retrieval of biomass combustion rates and totals from fire radiative power observations: FRP derivation and calibration relationships between biomass consumption and fire radiative energy release. Journal of Geophysical Research-Atmospheres 110, doi:https://doi.org/10.1029/2005jd006318.

Wooster, M.J., Zhukov, B., Oertel, D., 2003. Fire radiative energy for quantitative study of biomass burning: derivation from the BIRD experimental satellite and comparison to MODIS fire products. Remote Sensing of Environment 86, 83-107, doi:https://doi.org/10.1016/S0034-4257(03)00070-1.

Xu, W., Wooster, M.J., Roberts, G., Freeborn, P., 2010. New GOES imager algorithms for cloud and active fire detection and fire radiative power assessment across North, South and Central America. Remote Sensing of Environment 114, 1876-1895, doi:https://doi.org/10.1016/j.rse.2010.03.012.

Zhang, F., Wang, J., Ichoku, C., Hyer, E.J., Yang, Z., Ge, C., Su, S., Zhang, X., Kondragunta, S., Kaiser, J.W., 2014. Sensitivity of mesoscale modeling of smoke direct radiative effect to the emission inventory: a case study in northern sub-Saharan African region. Environmental Research Letters 9, 075002, doi:https://doi.org/10.1088/1748-9326/9/7/075002.

Zhang, X., Kondragunta, S., 2008. Temporal and spatial variability in biomass burned areas across the USA derived from the GOES fire product. Remote Sensing of Environment 112, 2886-2897, doi:https://doi.org/10.1016/j.rse.2008.02.006.

Zhang, X., Kondragunta, S., Ram, J., Schmidt, C., Huang, H.-C., 2012. Near-real-time global biomass burning emissions product from geostationary satellite constellation. Journal of Geophysical Research-Atmospheres 117, doi:https://doi.org/10.1029/2012jd017459.

Zhang, X., Kondragunta, S., Schmidt, C., Kogan, F., 2008. Near real time monitoring of biomass burning particulate emissions (PM2.5) across contiguous United States using multiple satellite instruments. Atmospheric Environment 42, 6959-6972, doi:https://doi.org/10.1016/j.atmosenv.2008.04.060.